

October 18, 1999 Revised version submitted to the *Journal of Geophysical Research*.

Microwave Limb Sounder observations of gravity waves in the stratosphere: A climatology and interpretation

Charles McLandress, M. Joan Alexander and Dong L. Wu

Abstract

Gravity wave activity in the stratosphere is inferred from high-horizontal-resolution temperature data from the Microwave Limb Sounder (MLS) on board the Upper Atmosphere Research Satellite. Global climatologies of temperature variance are computed using six years of observations in the solstice seasons. A linear gravity wave ray model is used to interpret the observations and to help determine whether information about the geographical distribution of gravity wave sources in the troposphere can be obtained. Realistic background wind and temperature fields which correspond to the MLS observing periods are used. The model variances are filtered in a manner which qualitatively simulates the instrument's response to wavelike temperature perturbations. Gravity wave source information is inferred by specifying a spatially-uniform momentum flux source spectrum in the troposphere and comparing the simulated results in the stratosphere to the observations. Spectra representing both convectively- and orographically-generated gravity waves are tested. The model is able to reproduce the zonal mean structure of the observations, indicating that the MLS data yield little information about the latitudinal dependence of gravity wave sources and are a reflection mainly of the background winds speeds whose variations at solstice are most pronounced in the meridional direction. Longitudinal variations of the observations in the summer hemisphere, however, are most certainly representative of variations in convective forcing since the model results exhibit much less variation in this direction. Simulations using the orographic spectrum exhibit large spatial variations as a result of critical level filtering by the background westerlies. This makes interpretation of the observed wintertime variances difficult. The large variances observed over the tip of South America, however, are most probably linked to orographic forcing since that is the only longitudinal sector containing any significant topography. The dependence of the observed variances on the viewing geometry of MLS is well-captured by the model. Information about ground-based phase speeds at source heights is embedded in the ascending-orbit descending-orbit variance ratios. Comparison of the model ratios to the observations suggests that the subtropical maxima in summertime is best represented by a relatively broad spectrum of gravity waves, while the midlatitude maxima in winter correspond to a much narrower spectrum.

1. Introduction

Over the past few decades it has become increasingly clear that gravity waves play a crucial role in controlling the large-scale circulation of the earth's middle atmosphere. Gravity waves are generated by a variety of different mechanisms and cover a wide range of temporal and spatial scales. Because of their ability to propagate upwards from the troposphere where they are forced, gravity waves can attain large amplitudes in the middle atmosphere as a result of the rapid fall-off in background density. At these heights the waves break, deposit their energy and momentum, and thus alter the background flow on which they propagate. Short horizontal-scale gravity waves are of particular concern to modelers who are trying to simulate the general circulation of the stratosphere and mesosphere, since they cannot be resolved by present-day global models. If their effects are not parameterized, however, the simulated winds become excessively strong and unrealistic.

Gravity wave parameterization is a complicated problem which requires not only an understanding of the physical mechanisms that cause the waves to break, but also the knowledge of wave sources in the troposphere. Although there has been considerable effort devoted to parameterizing the process of momentum deposition, there has been relatively little work done on parameterizing global wave sources. In the case of orographically-generated gravity waves this is relatively straightforward since topographic elevations are well known [e.g., *McFarlane*, 1987; *Bacmeister*, 1993]. However, for convectively-generated or shear-generated gravity waves the observations are insufficient to help constrain the parameterizations. As a consequence, modelers often prescribe horizontally uniform sources for the parameterized non-orographic gravity waves [see review by *McLandress*, 1998]. Clearly, there is a great need for more observations of gravity wave activity near the source regions.

Information about gravity wave sources can be inferred from horizontal wind and temperature variances in the troposphere and lower stratosphere, although variations in the background winds, static stability, and density scale height can make interpretation of these observations complex [*Eckermann*, 1995; *Alexander*, 1998 (hereafter A98)]. Long-term averages have been derived from radiosonde and rocket measurements [e.g., *Hirota*, 1984; *Tsuda et al.*, 1991; *Hamilton*, 1991; *Eckermann et al.*, 1994; *Allen and*

Vincent, 1995; *Nastrom et al.*, 1997]. Unfortunately these climatologies exist for only a limited number of geographic locations which are not evenly distributed around the globe. Satellite measurements therefore offer a means of supplementing these ground-based climatologies by providing global coverage. Global maps of temperature variance were first derived from Limb Infrared Monitor of the Stratosphere data [*Fetzer and Gille*, 1994]. Due to the nature of those observations, the results pertain to only the low frequency and long horizontal wavenumber portion of the gravity wave spectrum. Information about gravity waves of long vertical and short horizontal scale has recently been obtained using temperature data from the Microwave Limb Sounder on board the Upper Atmosphere Research Satellite (UARS) [*Wu and Waters*, 1996a; *Wu and Waters*, 1996b; and *Wu and Waters*, 1997] (henceforth WW96a,b and WW97). Although the MLS climatologies were generated using only several months of data, distinct geographical and seasonal patterns are clearly visible. For instance, large variances are observed over the continental land masses in the summer hemisphere in the sub-tropics and at mid-latitudes. Further evidence that the observed spatial patterns of temperature variance are due to gravity waves was given in WW97 who showed that the dependence of the MLS observations on the viewing geometry can only be reconciled with the notion that they are produced by vertically-propagating gravity waves.

Although it is tempting to ascribe horizontal variations in the observed variances to horizontal variations in the gravity wave sources, one must first consider the effects of the background atmosphere, since the observations are generally made several scale heights above the source regions. In addition, knowledge of the scale selectivity of the instrument is required since each observational technique measures only a limited portion of the entire gravity wave spectrum. These points are discussed in detail by A98, whose results demonstrate that the spatial and seasonal patterns of the observations can be explained in large part by the combination of wave-refraction and observational-filter effects. Since MLS is sensitive to long vertical wavelength disturbances, it is only in regions where winds are strong that gravity waves having slow or moderate ground-based phase speeds can be seen. This implies that horizontal variations in the background wind field alone can cause horizontal variations in the MLS temperature variances. Thus, in order to extract useful information about gravity

wave source variations, the impact of the background winds, as well as the instrument viewing geometry, must be carefully analyzed.

In this paper we focus exclusively on the MLS data and expand upon the results presented in WW96a,b and A98. The overall objectives are twofold: (1) to generate a climatology of the small-horizontal-scale temperature variance in solstice seasons from all of the available MLS data in the stratosphere throughout the 1992-1997 period and (2) to determine the degree to which these observations reflect variations in gravity wave sources in the troposphere. The paper is organized as follows: In Section 2 we present the observations. Here, we describe the MLS data and explain how the variances are computed. The effects of the viewing geometry are discussed and horizontal maps of the variance climatologies at the lowest observable altitude (38 km) are presented. Section 3 focusses on the interpretation of the observations using the linear gravity wave model of A98. A description of the model and its input source spectra, as well as the observational filter that is used, are presented. The conclusions and a brief summary of the results are presented in Section 4.

2. MLS Observations

2.1. Radiance Measurements

The data used in this study are optically-thick (or saturated) radiances from the rotational line emission from molecular oxygen at 63 GHz [Fishbein *et al.*, 1996]. The radiometer consists of 15 different channels and is designed so that the emission line is centered on channel 8, with the other channels being located symmetrically about the line center. For tangent heights $z_t < 18$ km the radiances for all channels are saturated, and so are indicative of atmospheric temperature¹ in the region where the emission originates. The altitude z_c where this occurs depends upon the channel number, with the center channel saturating at ~ 80 km and the wing channels 1 and 15 at ~ 28 km. (Figure 11, which will be discussed in detail later, provides a schematic representation of the viewing geometry.) Since measurements are made every 2 seconds, the horizontal distance between adjacent points is approximately 15 km (i.e., the distance travelled by the spacecraft in this

time interval). Thus, the saturated radiances provide a high-horizontal resolution dataset which spans the stratosphere and mesosphere at 8 different altitudes. It is important to note that the measured temperature does not correspond to an exact point in space but represents an average value which has been integrated over a three-dimensional volume of atmosphere. The shape and size of this averaging footprint depend upon the tilt of the instrument's line-of-sight (henceforth LOS), the width of the instrument's field-of-view (i.e., the antenna width), and the emission characteristics of the spectral channel. We will discuss this in greater detail in Section 3.2.

Saturated radiances from both the limb-scanning and limb-tracking observations are employed. In limb-scanning mode the atmospheric limb is scanned from 90 km to the surface. Here only the radiances at the bottom portion of each scan are saturated and thus useable for our gravity wave analysis. In limb-tracking mode the limb is viewed at a fixed height, which for $z_t < 18$ km yields a continuous set of useable measurements.

Temperature variances are computed as follows: For the limb-scanning data the method of WW96a is used. This entails removing a linear trend from the bottom six measurements of each 32-measurement scan and computing the variance from the resulting perturbations. This method, which retains horizontal scales < 90 km, will be referred to as the "six-point" method. In the limb-tracking case, the data are Fourier-filtered along the orbit track to retain only horizontal scales < 480 km (i.e., the approximate horizontal distance covered by the 32 measurements) and the variance is computed from the 32 filtered radiances. This will be referred to as the "480-km" method. Since the tangent height does not remain exactly fixed in limb-tracking mode, the radiances for the two pairs of wing channels (i.e., $z_c = 28$ and 33 km) may not be completely saturated. Consequently, only results for 38 km will be presented.

A typical day of scan or track radiance data yields approximately 1400 variance measurements per channel. Since the channels are symmetrically located about the line center, variances from opposite pairs of channels are combined. The variance is comprised of two components: atmospheric temperature fluctuations and instrument noise [WW96a]. Since the component due to noise is a constant for each channel, any temporal and spatial variations therefore reflect geophysical effects.

¹Microwave blackbody radiation is very nearly linearly proportional to temperature and is expressed in terms of "brightness temperature".

2.2. Variance Climatologies

Separate climatologies are computed for the four different viewing configurations, namely, north-looking ascending orbits, north-looking descending orbits, south-looking ascending orbits and south-looking descending orbits². A 5°-latitude by 10°-longitude grid is used to bin the daily variances and multi-year averages are computed for specified sets of months. The results are smoothed in both the latitudinal and longitudinal directions using a 1:2:1 three-point filter.

The scan and track datasets are treated separately since systematic differences exist between the two. This is demonstrated in Figure 1, which shows the zonal- and time-average track (dashed) and scan (solid) variances computed using the 6-pt method for the north-looking descending orbits for a time period when the two observing modes were used on alternate days. The differences between these two curves do not arise from geophysical differences in the datasets since the choice of the averaging period has minimized that, and so can only be attributed to the sampling differences associated with the two observing techniques. The 6-pt method should contain information on waves with horizontal wavelengths between ~ 15 -90 km. Comparing the two curves indicates that the 15-90 km variance in the 6-pt track data is small and barely distinguishable from the noise level³, while the scan data has significant signal at high northern latitudes and near 20°S. When the track variances are instead computed using the 480-km method (dotted) the variance now includes horizontal wavelengths ~ 15 -480 km and the result is very similar to the scan data. This indicates that most of the variance in the MLS data is due to waves with horizontal wavelengths > 90 km. The scan data must therefore be detecting vertical variations in the temperature associated with longer horizontal wavelength waves (~ 90 -480 km). Despite using only six points, the large variances appear due to aliasing of the vertical variations in the scan data associated with the varying elevation angle of the LOS. These systematic differences can also be

seen in the scan and track variances shown in WW96a and b. Henceforth, any reference in this paper to limb-tracking variances implies those calculated using the 480-km method.

Variance climatologies at 38 km are generated for the north- and south-looking periods of December, January and February (DJF) and June, July and August (JJA). The total number of days of limb-scanning and limb-tracking observations that are used in constructing these climatologies is listed in Table 1. The bulk of the data is seen to be limb scanning, which was the mode used from launch in September 1991 until July 1997 when the 63-GHz radiometer was turned off. The limb-tracking mode was not employed until December 1994; it was used exclusively until April 1995 after which it alternated with limb-scanning observations.

The dependence of the latitudinal structure of the variances on the instrument's viewing geometry is demonstrated in Figure 2, which shows the zonal-average variances for the north-looking days of DJF and the south-looking days of JJA. Large differences between the ascending- and descending-orbit (henceforth AD) variances are clearly seen. The limb-tracking variances in the northern hemisphere winter are nearly a factor of two larger on the descending orbits (dashed) than on the ascending orbits (solid). South of the equator in DJF (southern hemisphere summer in the subtropics) the ascending-orbit results are larger but only by about 30%. This picture is reversed in JJA when MLS is south-looking. These results indicate that the largest variances occur when the instrument LOS has an eastward component in wintertime and westward in summertime. A98 discussed the relationship between the variance in these observations and the background wind. Since MLS is sensitive to only long vertical wavelength disturbances, regions where the winds are strong are where gravity waves of low to moderate ground-based phase speeds c are most observable. This follows from the approximate gravity wave dispersion relation $m^2 \approx N^2/(U - c)^2$, which indicates that the vertical wavenumber m is inversely proportional to the intrinsic phase speed, $U - c$, where U is the background wind and N is the buoyancy frequency. Such waves will have phase fronts that tilt westward with height in winter and eastward in summer. For example, during north-looking periods in winter, the descending orbits contain more variance since the LOS is oriented northeastward (and downward) throughout the middle portions of the orbit and thus is more

²Ascending and descending refer to orbit segments where latitude increases and decreases, respectively, with increasing universal time; north- and south- looking refer to the spacecraft orientation, which rotates every 36 days and provides latitudinal coverage that ranges from 35°S to 80°N and from 80°S to 35°N.

³The flat structure at low latitudes in the winter hemisphere is indicative of the contribution from instrument noise, which for channels 3 and 13 is estimated at $\sim 0.01^\circ\text{K}^2$ (Table 1 of WW96b). Note that the noise has not been removed from any of the figures.

parallel to the wave phase fronts than on ascending orbits. Table 2 provides a summary of the viewing geometry which will aid in the interpretation of the results. The scan variances (Figure 2b) are similar in structure but exhibit smaller AD differences at high latitudes in winter and larger differences at low latitudes in summer. As will be discussed later when we present the model results, a large part of the latitudinal and seasonal patterns seen here is more a reflection of the background winds and the observing characteristics of MLS than of actual variations in gravity wave sources.

The geographical patterns of the track and scan temperature variances are shown in Figures 3 to 5. Each of the four panels in these figures constitutes an independent climatology corresponding to the time periods listed in Table 1. For conciseness, only results for the viewing configuration that yields the largest variances are presented. The summer hemisphere scan and track variances (Figures 3 and 4) exhibit very similar spatial structure. The maxima in both datasets are situated squarely over the subtropical continents: In JJA they occur over Africa and south east Asia at $10\text{--}15^\circ\text{N}$ and over North America at 30°N , while in DJF they lie over south central Africa, northern Australia and central South America at 20°S . In addition, the region of large variance over North America is seen to extend further northward than over Africa and Asia. A $5\text{--}10^\circ$ shift in the latitude of the maxima between the north- and south-looking periods is also evident. Although the reason for this southward shift may be geophysical, it is more likely that geometric differences resulting from the changes in the orientation of the instrument's LOS are responsible. The winter hemisphere data are shown in Figure 5. In the southern hemisphere large variances are found over the tip of South America and the Antarctic Peninsula for both the track and scan climatologies. In the northern hemisphere the correspondence between the two datasets is not as strong: although the largest values are still found over the continents at high latitudes, the locations of the individual maxima differ. The fact that the scan variances tend to exhibit smoother horizontal variations than the track data, is a consequence of the length of the two datasets. For example, the sharp peak in the track variances over central North America near 40°N seen in Figure 3a is associated with large values occurring along a single orbit track.

As discussed in A98 background winds play an important role in determining the spatial variation of the

MLS temperature variances. Figure 6 shows the time-average large-scale horizontal winds at 38 km from the U.K. Meteorological Office (UKMO) assimilated dataset which provides gridded winds and temperatures for each day of the UARS mission [Swinbank and O'Neill, 1994]. The wind climatologies shown here have been computed from the same set of days used in generating the limb-tracking variances for the north-looking days of DJF and the south-looking days of JJA. In southern hemisphere summer the latitudinal distribution of the variances (Figure 4a) closely matches that of the background easterlies, with the largest variances occurring at the latitudes where the winds are strongest. Although the same occurs in northern hemisphere summer over Asia and Africa (Figure 3b), the relatively large variances over North America are not associated with strong winds. This suggests the presence of gravity waves with high ground-based phase speeds since those will be the waves having long vertical wavelengths. The correspondence between the winds and variances is most evident in the northern hemisphere winter where the winds are strongest and exhibit the greatest longitudinal variation. Note, for instance, the weak variances over North America (Figure 5b) where the winds are weak and the large values over eastern Russia where the winds are strong.

Temporal variations in gravity wave activity can provide information about source intermittency. Figure 7 shows the standard deviations of the variances about the time means shown in Figures 3-5. Since there are fewer limb-tracking days, only scan variance deviations have been presented. In summertime the geographical distribution of the deviations is nearly the same as the means. Subtle differences in the positions of the maxima are seen over central South America where the maximum deviations occur about 5° further south than the maximum means. Although the winter hemisphere standard deviations are similar in overall structure to the corresponding mean values, there exists greater geographic variability; this is particularly true over North America. Note also that in regions where the mean variances are large the standard deviations are as large or larger, which indicates that the small-scale temperature field exhibits a high degree of temporal variability. For example, over the Antarctic Peninsula standard deviations of approximately 0.25°K^2 occur, in contrast to a mean value of 0.09°K^2 . Over the continents in summertime, the deviations are smaller and about the same size as the means. Whether these results are indicative of tem-

poral variations of the gravity wave sources in the troposphere will depend to a large extent upon the temporal variations of the background winds in the stratosphere. The significance of these results will be discussed in the next section when we present the model results.

The high degree of correlation between the MLS observations shown in Figures 3-5 and 7 and the continental land masses suggests the presence of geographically-fixed gravity wave sources in the troposphere. Two obvious candidates are deep convection in summer and forced flow over mountains in winter. In Figure 8 are shown longitudinal variations of the MLS track and scan temperature variances and time-average outgoing longwave radiation (OLR) at 15°N for JJA and 15°S for DJF. (The OLR data are taken from the National Center for Atmospheric Research archive of twice-daily AVHRR soundings [Liebmann and Smith, 1996].) The MLS observations show a striking correspondence with the occurrence of deep convective clouds (indicated by low values of OLR), which has also been noted in previous observations of gravity wave activity [Rottger, 1980; Larsen *et al.*, 1982; Sato *et al.*, 1995; Alexander and Pfister, 1995]. Figure 9 shows the MLS data in winter at 55°S and 55°N and the corresponding subgrid-scale orographic height field used in the gravity wave drag parameterization of McFarlane [1987] in the version of the Canadian Middle Atmosphere Model described in McLandress [1998]. The peak in the MLS variances in the southern hemisphere winter at ~ 60°W corresponds quite well with the rough terrain over the southern tip of the Andes. The eastward displacement of the variance maximum may be a manifestation of mountain waves on the lee side of the Andes [e.g., Eckermann and Preusse, 1999], as well as the 10° bin size of the dataset. In the Northern Hemisphere the correspondence between rough terrain and the MLS variances is not as clear, which suggests that gravity waves from other sources may be present. To help quantify the relationship between the MLS temperature variances in the stratosphere and gravity wave sources in the troposphere, we now resort to numerical simulations.

3. Linear Gravity Wave Model

The linear gravity wave model described in A98 is used to aid in the interpretation of the MLS temperature variances. The model simulates a spectrum of vertically-propagating gravity waves: it includes the effects of rotation, non-hydrostaticity and linear

wave saturation; it requires an input momentum flux source spectrum, an efficiency factor which accounts for the spatial and temporal intermittency of the gravity wave sources, and a background wind and temperature field on which the waves propagate. The computed temperature variances are then filtered in a manner which simulates the MLS observations. Unlike more sophisticated models [e.g., Marks and Eckermann, 1995], this one does not account for the horizontal displacement of ray paths. This is not a serious omission, however, since the gravity waves that are observable by MLS have high intrinsic frequencies and therefore propagate nearly straight up.

The degree to which the MLS observations reflect horizontal variations of gravity wave sources in the troposphere depends to a large extent upon the effects of filtering and wave refraction by the background winds as the waves propagate upward into the stratosphere. In order to determine the impact of the background winds and temperatures, we will follow the procedure of A98 and prescribe a globally uniform momentum flux source spectrum. Horizontal variations which are not simulated by the model will therefore suggest that the observations do indeed reflect the geographic pattern of the underlying sources. Since there is a high degree of uncertainty in both the shape and azimuthal dependence of the source spectrum, experiments using several different types of spectra will be performed.

3.1. Model Configuration

The configuration of the model is somewhat different from that used in A98 where only zonally-propagating waves were considered. Here, we retain the two-dimensional dispersion relation used in A98

$$\omega^2 = \frac{N^2 k^2 + f^2(m^2 + \alpha^2)}{k^2 + m^2 + \alpha^2} \quad (1)$$

where ω is the intrinsic frequency, k is the horizontal wavenumber, f is the Coriolis parameter, $\alpha = 1/(2H)$, and H is the density scale height. Unlike A98 we allow for arbitrary horizontal directions of propagation. The background wind in each azimuth is therefore given by

$$U_j = U \cos \alpha_j + V \sin \alpha_j, \quad (2)$$

where α_j is the angle of the j -th azimuth measured from east, and U and V are the eastward (zonal) and northward (meridional) wind components, respectively.

Two basic types of momentum flux source spectra $F_{P0}(c, k)$ are examined: The first consists of a

horizontally-isotropic broad spectrum of waves having zero flux at $c = 0$. This will be referred to as the “broad spectrum” and can be considered to include sources like convection and shear instability which may produce waves with a wide range of frequencies, wavelengths and propagation directions. The second consists of a horizontally-anisotropic spectrum that is very narrow in phase speed and has the largest flux at $c=0$. This will be referred to as the “narrow spectrum” and is meant to represent waves from sources like flow over orography.

In the simulations employing the broad spectrum, twelve equally-spaced horizontal azimuths are used. To ensure that the source is truly horizontally uniform, a zero background wind and a constant buoyancy frequency are prescribed at the 6-km source level. These are blended in smoothly with the spatially-varying atmosphere above in the manner used by A98. Since there are virtually no observations of the phase speed distribution of nonorographic gravity waves, three different spectral shapes are tested: The first is one in which each wave is assigned the same momentum flux and will be referred to as the “flat spectrum”. A total of 56 waves, having horizontal wavelengths of 6.25, 12.5, 25, 50, 100, 200, 400 and 800 km and periods of 15, 20, 24, 30, 60, 120 and 240 minutes, are specified in each azimuth. The flat spectrum is further restricted to waves whose phase speeds are less than 170 m/s. This reduces the total number of waves in each azimuth to 46 which yields a grand total of 552 waves for all twelve azimuths. F_{P0} and the efficiency factor ϵ are determined from observational constraints on the momentum flux divergence in the manner described by *Alexander and Rosenlof* [1996]. Here, we use $F_{P0} = 0.1957 \text{ m}^2\text{s}^{-2}$ and $\epsilon = 9 \times 10^{-5}$, which yields a total integrated “long term” momentum flux $F_{P_{tot}}$ (i.e., $F_{P_{tot}} = \epsilon \Sigma F_{P0}$) at the source height of $2.7 \times 10^{-3} \text{ m}^2\text{s}^{-2}$ in each azimuth. Note that momentum flux is defined here as the covariance of the horizontal and vertical wind components and does not contain the density factor. Apart from the use of twelve azimuths (and the associated change in ϵ) this configuration is identical to the one used in A98. The two other broad spectra are given by the functional form used in *Alexander and Dunkerton* [1999], i.e.,

$$F_{P0}(c, k) = \text{sgn}(c_i) B_m \exp \left[- \left(\frac{c}{c_w} \right)^2 \ln 2 \right], \quad (3)$$

where c_i is the intrinsic phase speed at the source level, $B_m = 0.2 \text{ m}^2\text{s}^{-2}$, and c_w is the spectral width.

For simplicity, F_{P0} has been assumed to be independent of k . Each azimuth contains 48 waves having horizontal wavelengths of 25, 50, 100, 200, 400 and 800 km and phase speeds varying from $0.5\Delta c$ to $3c_w$ ($\Delta c = 0.4c_w \text{ m/s}$). Spectral widths of $c_w = 20$ and 50 m/s are prescribed. Settings of 3×10^{-4} and 2.7×10^{-4} are used for ϵ for the $c_w = 20$ and 50 m/s cases, respectively. These values yield a total momentum flux in each azimuth which is nearly identical to that of the flat spectrum.

The momentum flux distribution for the narrow spectrum is given by Eq (3) using $B_m = 1 \text{ m}^2\text{s}^{-2}$ and $c_w = 1 \text{ m/s}$. The source level is set at 3 km. Unlike the simulations using the broad spectra, the background winds and buoyancy frequency are not altered at the source level and wave propagation is confined to only a single horizontal azimuth, namely the azimuth opposite to the source level wind vector. Note that this configuration corresponds to the propagation direction used in orographic gravity wave drag parameterizations that assume horizontally isotropic sub-gridscale topography [e.g., *McFarlane*, 1987]. A total of 52 waves are used, having horizontal wavelengths of 50, 100, 200 and 400 km and ground-based phase speeds ranging from -3 to $+3 \text{ m/s}$ ($\Delta c = 0.5 \text{ m/s}$) and ϵ is set to 5×10^{-4} . These settings yield a zonal force of $\sim -100 \text{ ms}^{-1}\text{day}^{-1}$ in the winter mesosphere and $\sim -2 \text{ ms}^{-1}\text{day}^{-1}$ above the winter tropospheric jet when the COSPAR International Reference Atmosphere (CIRA) [*Fleming et al.*, 1990] zonal mean winds and temperatures are used.

Since model calculations are performed in terms of the vertical velocity amplitude squared (E_w), the momentum flux at the source height must be recast in those terms. This is done using the linear dispersion relation Eq (1) and the polarization relations [*Gossard and Hooke*, 1975, pp. 97-100] which yields

$$E_{w0} \approx 2 \left[\frac{\omega_0^2 - f^2}{N_0^2 - \omega_0^2} \right]^{1/2} |F_{P0}|, \quad (4)$$

where the subscript “0” denotes the source level. In the case of the narrow spectrum, E_{w0} is constrained to not exceed the convective instability limit $E_{wb0} = \omega_0^2/m_0^2$ as done in orographic gravity wave drag parameterizations [e.g., *McFarlane*, 1987]. For the broad spectra, waves whose amplitudes exceed E_{wb0} are simply excluded from the calculations to be consistent with A98. As a result of the modifications to the low-level winds and buoyancy frequency, E_{w0} for the broad spectra is nearly horizontally uniform with a very weak latitudinal dependence due

to f . E_{w0} for the narrow source spectrum, however, has a strong spatial dependence which is given by $E_{w0} \approx 2kU_0N_0^{-1}F_{P0}$, where U_0 is the background wind in the direction opposite to the direction of wave propagation.

The background atmospheres which are employed in all subsequent model results are specified using the UKMO winds and temperatures. The data used here are given on a 4° by 5° latitude-longitude grid and have 22 pressure levels ranging from 1000 to 0.3 hPa, which are interpolated to a log-pressure vertical grid having a 1-km resolution. The UKMO climatologies are constructed using the days corresponding to the MLS limb-tracking observations given in Table 1. The time-average UKMO data for the north-looking days of DJF and the south-looking days of JJA will henceforth be referred to as the DJF-N and JJA-S background atmospheres, respectively. The corresponding zonal mean zonal winds are shown in Figure 10.

Vertical profiles of the temperature perturbation T are computed for each wave in the spectrum and for each azimuth. The model temperatures are filtered in wavenumber space using an observational filter \mathcal{F} appropriate for MLS and then summed to yield the simulated “observed” temperature variance V_{obs} . Since MLS is only sensitive to long vertical wavelength gravity waves, which propagate rapidly through the stratosphere, the time-average variances will be strongly affected by the intermittency of the gravity wave sources as is discussed in A98. Consequently,

$$V_{obs} \propto \epsilon \sum_{j,k,m} \mathcal{F}_j(k,m) T_j^2(k,m), \quad (5)$$

where the proportionality sign has been used to indicate that the intermittency scale factor (ϵ) is somewhat arbitrary. Note that for comparison purposes, the filtered model variances that will be shown are also multiplied by a constant of order one. The observational filter which is used in simulating the MLS observations will now be discussed.

3.2. Observational Filter

The observational filter that was used in A98 to interpret the MLS limb-scanning temperature variances of WW96a consists of a Gaussian-shaped low-pass vertical-wavenumber filter and a horizontal-wavenumber filter that selects only short spatial scales. This two-dimensional filter does not take into account the orientation of the instrument LOS, which is responsible

for the viewing direction dependencies seen in Figure 2. Here, we describe in detail a three-dimensional wavenumber filter which does.

The coordinate system that is used to define the filter is depicted in Figure 11: The origin is located along the “data track”, which is the path traced out by the saturated radiance measurements. The “across-track” direction (y) is perpendicular to the data track and is aligned with the LOS; the “along-track” direction (x) is parallel to the data track and is positive in the direction of satellite motion. The “track angle” (α_T) is the angle measured counterclockwise from East to the x -axis. The vertical coordinate is denoted by z . We restrict ourselves to the limb-tracking configuration, since the vertical tilt of the LOS is fixed.

An idealized two-dimensional weighting function W_{yz} is constructed from the height-dependent weighting function W_z in a manner similar to that used by WW97. As in A98, we approximate the W_z ’s shown in Figure 2 of WW96a using

$$W_z = \exp \left[- \left(\frac{z}{w_c} \right)^2 \right], \quad (6)$$

where $z = z^* - z_c$, z^* is the height above the earth’s surface, $z_c = 38$ km and $w_c = 6.8$ km. W_{yz} is expressed analytically as

$$W_{yz} = W_z(z) \exp \left[- \left(\frac{z - y\beta}{w_b} \right)^2 \right], \quad (7)$$

where $\beta = -\cos^{-1}[(r_e + z_t)/(r_e + z_c)]$ is the angle between the LOS and the y -axis, r_e is the earth radius, $z_t = 18$ km is the tangent height and $w_b = 4.9$ km represents the width of the instrument antenna at z_c .⁴ The resulting two-dimensional weighting function for channels 3 and 13 is depicted on the left-hand-side of Figure 12a. Note that W_{yz} has been constructed so that its horizontal average is proportional to W_z as can be seen by integrating Eq (7) from $y = \pm\infty$. Constructing W_{yz} in this manner enables a direct comparison to the results of A98, since the vertical wavenumber response for a disturbance having an infinitely long across-track horizontal wavelength is identical to that obtained using only the height-dependent weighting function W_z . By a transforma-

⁴The vertical half-power beam width is 0.206° [Jarnot *et al.*, 1996, Table 3]. Changes in the beam width along the LOS have been ignored and are instead replaced by a constant value at the origin.

tion of coordinates, Eq (7) can be rewritten as

$$W_{yz} = \exp \left[- \left(\frac{y'}{w_{y'}} \right)^2 \right] \exp \left[- \left(\frac{z'}{w_{z'}} \right)^2 \right], \quad (8)$$

where $y' = y \cos \phi + z \sin \phi$, $z' = -y \sin \phi + z \cos \phi$,

$$w_{y'} = \frac{w_c}{\sqrt{\sin^2 \phi + \gamma (\sin \phi - \beta \cos \phi)^2}},$$

$$w_{z'} = \frac{w_c}{\sqrt{\cos^2 \phi + \gamma (\cos \phi + \beta \sin \phi)^2}},$$

$$\tan 2\phi = \frac{2\beta}{1 - \beta^2 + \gamma^{-1}},$$

and $\gamma = (w_c/w_b)^2$. This coordinate system rotation aligns the y' -axis along the major axis of W_{yz} . The across-track temperature response function is now simply the normalized Fourier transform of Eq (8), which is given by

$$R_{yz} = \exp \left[- (\pi w_{y'} k_{y'})^2 \right] \exp \left[- (\pi w_{z'} k_{z'})^2 \right], \quad (9)$$

where $k_{y'} = k_y \cos \phi + k_z \sin \phi$ and $k_{z'} = -k_y \sin \phi + k_z \cos \phi$. Note that the wavenumber is expressed in units of cycles per km; thus inverse wavenumber equals wavelength. Figure 12b shows the temperature response given by Eq (9) as a function of the across-track and vertical wavenumbers, k_y and k_z . Since k_z is positive by definition here, waves with $k_y < 0$ have phase lines which are more perpendicular to the LOS and so are strongly attenuated. In addition, the response for waves with $k_y < 0$ exhibits a monotonic decrease with increasing k_z , indicating that the longest vertical wavelengths are most visible. At $k_y = 0$ the vertical wavenumber response is identical to that used in A98. Waves with positive k_y , however, have phase lines which are more aligned with the LOS and so undergo less attenuation. Moreover, the response is no longer monotonically decreasing: For example, a wave with a 250-km across-track wavelength has the largest response when its vertical wavelength is ~ 20 km. Note also that as the vertical wavelength increases, the response becomes more symmetric about $k_y = 0$.

In the along-track direction, the response at short wavelengths is determined by the combined effects of smearing due to the 2-second integration time and the finite width of the horizontal beam whose half-power beam width $\sim 0.4^\circ$ [Jarnot et al., 1996]. At long wavelengths the response is determined by the

numerical technique that is used to compute the variances. Since we are simulating the 480-km track data, a wavelength cutoff at 480 km is therefore imposed. Thus, the along-track temperature response shown in Figure 12c is approximated as

$$R_x = \exp \left[- (\pi w_x k_x)^2 \right] \quad \text{for } k_x > 1/(480 \text{ km}), \quad (10)$$

where $w_x = 10$ km, and $R_x = 0$ for $k_x < 1/(480 \text{ km})$.

The total response of a monochromatic wave is simply the product of the responses given by Eqs (9) and (10). The across- and along-track horizontal wavenumbers are calculated from the corresponding values in the earth-based coordinate system with aid of the track angle α_T , whose latitudinal dependence is shown in Figure 12d for the four different viewing configurations. Consider, for example, a westward-propagating wave at 56°S having horizontal and vertical wavelengths of 200 and 20 km, respectively. Assuming that the wave's group velocity is upward, its phase fronts will be tilted westward with height. For south-looking ascending-orbit geometry $\alpha_T = 54^\circ$, i.e., the LOS is pointing southeastward. This yields $k_x \sim 1/(340 \text{ km})$ and $k_y \sim 1/(250 \text{ km})$, which from Figures 12b and 12c gives $R_{yz} \sim 0.55$ and $R_x \sim 1$ for a total squared-amplitude response $\mathcal{F} \sim 0.3$. For descending-orbit geometry $\alpha_T = -54^\circ$ and so $k_y \sim -1/(250 \text{ km})$. This yields $R_{yz} \sim 0.006$ and $\mathcal{F} \sim 3 \times 10^{-5}$, which is four orders of magnitude weaker than that for the ascending-orbit configuration.

Note that in simulations using twelve horizontal azimuths, the first azimuth is aligned parallel to the data track in the positive x -direction, with the angle α_j given in Eq (2) being positive in the counterclockwise direction. This is done in order to prevent spurious latitudinal variations in the filtered variance that would arise if the azimuths were oriented in a fixed geographic direction.

It should be pointed out that Eq (7) is an approximation of the true weighting function whose spatial structure is not easily computed. Although it would be qualitatively similar to the one shown in Figure 12a, the actual weighting function would not have a simple analytical wavenumber response function suitable for use in the model. However, in light of the other simplifications inherent in the model, the development of a more complicated filter does not seem warranted.

Examination of Figure 12 also reveals why it is difficult to construct a simple filter that would be appropriate for the limb-scanning observations. In

limb-scanning mode, the vertical tilt angle of the instrument LOS changes with each measurement in the scan, varying from $|\beta| \sim 4.5^\circ$ ($z_t = 18$ km) to $\sim 6.2^\circ$ ($z_t = 0$ km) for channels 3 and 13. This greatly complicates matters since it couples the across-track and along-track responses.

3.3. Model Results

In the first section we examine the zonal mean results computed using the different source spectra. This provides a compact means of demonstrating the characteristics of the filter and of comparing the latitudinal variations of the simulations to the observations. In the second and third sections we focus on longitudinal and temporal variations at specified latitudes. Note that all calculations are performed on the longitude grid, and that all simulations employ north- and south-looking geometry in conjunction with the DJF-N and JJA-S background atmospheres, respectively.

3.3.1. Zonal means. Figure 13 shows the zonal-average temperature variances computed using the flat spectrum. The solid and dashed lines denote the results for the ascending- and descending-orbit configurations of the filter, respectively, while the dotted lines depict the corresponding unfiltered variances calculated using Eq (5) with $\mathcal{F} = 1$. Unlike the filtered variances which are weak in the tropics, the unfiltered variances are relatively strong there. (Note also that the unfiltered variances are an order of magnitude larger than the filtered ones.) The filtered variances are largest where the background winds are largest (Figure 10). In addition, the AD differences resemble the observations seen in Figure 2, although they are smaller than in the observations. As discussed in Section 2.2 this occurs for the following reasons: North of 15°N , where zonal mean westerlies are present in the DJF-N atmosphere, gravity waves with westward intrinsic phase speeds dominate. Since upward propagating waves have phase lines which tilt westward with height, the largest response occurs along the descending orbits when the LOS is pointing northeast (see Table 2), which is the situation shown in Figure 11. In this configuration the LOS is more often oriented directly along the wave phase lines, in contrast to the other viewing direction in which the two are more often perpendicular. Similarly, south of 15°N the presence of zonal mean easterlies results in the predominance of upward-propagating waves with eastward intrinsic phase speeds, which tilt eastward with height and so are more visible when viewed on

the ascending orbits. For the JJA-S atmosphere, the exact opposite occurs since south-looking geometry is used.

The filtered variances depend strongly upon the horizontal propagation directions of the gravity waves as is demonstrated in Figure 14 which shows the zonal mean variances computed using the flat spectrum for the subtropics in summer and at high latitudes in winter. Comparison of the ascending orbits (solid) and descending orbits (dashed) indicates that waves with horizontal components of propagation perpendicular to the LOS are most visible. The anisotropy that results directly from background wind filtering is seen by the dotted curves which show the unfiltered results. Note that the sum of the variances at all azimuths yields the values shown in Figure 13.

The zonal-average filtered variances for the $c_w = 20$ and 50 m/s spectra are shown in Figure 15. The latitudinal structure of the variance is now seen to coincide closely with the strongest winds shown in Figure 10. Like the observations in Figure 2, the variances in wintertime are largest in the southern hemisphere where the winds are undistorted by planetary waves and the zonal means are stronger. Note that the summertime maximum at 20°S is somewhat more pronounced than in the northern hemisphere summer as a result of the stronger zonal easterlies. Comparison to the results using the flat spectrum also reveals an increase in the latitudinal variation as the width of the spectrum decreases, which is in closer agreement with the observations. Furthermore, as c_w decreases the difference between the AD variances increases. This occurs because decreasing c_w also decreases the average vertical wavelength of the spectrum, which results in the increased asymmetry of the across-track wavenumber response as seen in Figure 12b. We will return to this point shortly.

The zonal-average variances computed using the narrow source spectrum are shown in Figure 16. The results for the descending- and ascending-orbit configurations of the filter in panels (a) and (b), respectively, are several orders of magnitude smaller and so are not shown. In contrast to the previous results, the variances for the narrow spectrum are much more sharply peaked in latitude in better agreement with the observations at mid and high latitudes (Figure 2). Critical-level filtering in the vicinity of the zero-wind line in the summer stratosphere (Figure 10) plays an important role by confining the waves to the winter hemisphere as can be seen by the latitudinal structure of the unfiltered variances (dotted lines). Com-

parison of the filtered and unfiltered results indicates that only waves propagating through regions of very strong background winds will be visible through the filter. Consequently, gravity waves which are generated over mountainous terrain at lower latitudes where the background winds are weaker (e.g., the northern Andes or the Himalayas) would not be observable by MLS.

The above model results also suggest that the differences between the AD variances in the MLS data may provide some insight into the dominant vertical wavelengths (and hence phase speeds) which are present in the actual source spectrum. A comparison of the observed limb-tracking and model variance ratios is presented in Table 3. Note that the variances for the westward-looking view in the summer hemisphere and the eastward-looking view in the winter hemisphere are used as the numerators in the ratios. Here, model ratios denote zonal averages, while the observations show both the zonal mean and the value at the location of the variance maximum. In computing the observed variance ratios, the instrument noise, which has been estimated from Figure 2, has first been subtracted off. Note that the actual values will be somewhat sensitive to the assumed noise floor. Of the three model spectra, the $c_w = 50$ m/s spectrum more closely reproduces the observed ratios at low latitudes in the summer hemisphere, while the narrower $c_w = 20$ m/s spectrum better matches the observations at high latitudes in the winter hemisphere. (The ratios for the narrow spectrum are not presented because those waves are effectively visible on only one half of the orbit track, i.e., either ascending or descending.) Note that if the spectral shapes are very different from what we have assumed, then the inferences about the widths of the phase speed spectrum from these ratios can only be made qualitatively. Furthermore, if the wave sources are highly anisotropic, then these comparisons may not be meaningful. However, recent satellite measurements of high-frequency convectively-generated gravity waves show a concentric pattern of wave fronts radiating away from the storm [Dewan *et al.*, 1998], which provides some evidence that such waves are horizontally isotropic near the source levels.

3.3.2. Longitudinal structure. Let us now turn our attention to the longitudinal structure of the variances. For conciseness, we will only consider the latitudes corresponding to the maximum observed variances shown in Figures 3-5. As before, results are presented for the filter configuration that yields the

largest variance for the latitude and season in question. Figure 17 shows the filtered variances for the flat (solid curve) and $c_w = 20$ m/s (thick dashed-dotted curve) source spectra, as well as the MLS limb-tracking observations (gray curves), at four different latitudes. The flat spectrum, which contains the higher phase speed waves and hence the longer vertical wavelengths, exhibits less longitudinal variation since the ability to observe these waves is less affected by changes in the background winds (see Figure 6). As the spectral width decreases, the waves in the observable vertical wavelength range become more closely tied to background wind speeds, which explains why the longitudinal variation of the $c_w = 20$ m/s results is greater. Results for the $c_w = 50$ m/s spectrum fall between these two curves and so are not shown.

The results using the narrow spectrum are shown in Figure 18 at 56°S and 56°N for wintertime. The model variances exhibit strong variations in longitude, especially in the Northern Hemisphere where large-amplitude quasi-stationary planetary waves distort the background wind. Note, for instance, at 56°N how the filtered variances are negligible between 120°E and 90°W . This results from the combined effects of the longitudinal variations in the background winds, E_{w0} , and wave breaking in the lower stratosphere.

The degree to which the MLS observations reflect longitudinal variations in gravity wave sources depends to a large extent upon the structure of the background mean winds and the phase speed characteristics of the assumed source spectrum. In the subtropical summer stratosphere, the time-average background atmosphere is nearly zonally symmetric due to the absence of quasi-stationary planetary waves (Figure 6a,b). Consequently, the filtered results computed using the broad source spectra exhibit much less longitudinal variation than do the observations, which is further evidence that the observed maxima over Asia and North America at 12°N in JJA and over Africa, Australia and South America at 20°S in DJF are indicative of regions of stronger forcing of gravity waves.

In the southern hemisphere winter at 56°S the broad-spectra model results exhibit relatively little longitudinal variation. Consequently, the observed maximum over the tip of South America must clearly be associated with a region of localized gravity wave generation. Figure 18a indicates that the most likely forcing mechanism is by flow over orography since this is the only longitudinal sector in the vicinity of moun-

tainous terrain as can be seen from Figure 9c. However, the presence of relatively large variances over the oceanic sectors in Figure 5c indicates that sources other than topography are active at these high latitudes. The fact that the AD ratios at these longitudes (results not shown) are significantly larger than unity suggests that these waves have relatively slow ground-based phase speeds.

The northern hemisphere wintertime results are more difficult to interpret. Due to the presence of large-amplitude planetary waves in the background atmosphere (Figure 6d), the results using both the broad and narrow source spectra (Figures 18b and 17d) show large spatial variations. This indicates that the MLS observations contain little information about the spatial structure of gravity wave sources in the Northern Hemisphere winter. The fact that the observed maximum at 120°E lies above regions of rough terrain (Figures 9b and 9d) is suggestive of orographic forcing. However, the model results computed using the narrow spectrum show only a weak amplitude response as a result of the weak source-level winds at these longitudes. At 56°N a broader spectrum of phase speeds (e.g., $c_w = 20$ m/s) appears to better fit the observations. Like the southern hemisphere wintertime results, the presence of large AD variance ratios in the northern hemisphere winter suggests that a relatively narrow spectrum of phase speeds is present but not as narrow as over the southern Andes.

3.3.3. Temporal intermittency. In order to examine the impact of the time-dependent background atmosphere on the time-average variances, the daily UKMO winds and temperatures that were used in generating the JJA-S and DJF-N climatologies are employed. The filtered variances are calculated for each day and the time-average is computed. In the case of the $c_w = 20$ m/s spectra (thin dash-dotted lines in Figure 17), temporal variations in the background atmosphere do not have a significant impact on the time-average variance. (Those using the flat spectrum bear a very close resemblance to those computed using the time mean winds and temperatures and so are not shown.) In the narrow spectrum case (thin solid lines in Figure 18), however, use of the time-varying atmosphere has significantly modified the longitudinal structure of the time-mean variances, resulting in a reduction of the peak magnitude of the filtered variances by at least a factor of two. Thus, temporal variations become increasingly more important as the range of ground-based phase speeds in the source spectrum is reduced. These results indicate that the

day-to-day variability of the background winds can have a large impact on the time-average variances in the case of the narrow anisotropic spectrum, a result that has previously been shown by *Dunkerton and Butchart* [1984] in the context of stationary gravity wave propagation during sudden stratospheric warmings.

These model results suggest that the large values of the standard deviations of temperature variance observed over the subtropical continents in summer (Figure 7a,b) do not arise from changes in the mean winds and temperatures and so are a reflection of temporal variations of the wave sources in the troposphere. (It should be pointed out that temporal intermittency in this case may include not only variations in wave amplitude but also wave directions.) The variability at high latitudes in winter (Figure 7c,d), however, does not appear to yield information about gravity wave source intermittency since it can also result from temporal variations in the background winds.

4. Summary and Conclusions

We have presented an analysis and interpretation of gravity-wave-scale temperature variances in the stratosphere using data from the Microwave Limb Sounder's 63-GHz radiometer on board the Upper Atmosphere Research Satellite. The variances are derived from optically-thick limb radiances that have a horizontal resolution of ~ 15 km along the orbit track. Climatologies of mean variance, as well as the standard deviation about the means, are generated for the solstice seasons. The datasets provide near-global coverage at eight different altitudes in the stratosphere and mesosphere. In this paper results at only 38 km are presented.

MLS is sensitive to only long vertical wavelength disturbances. The observable horizontal scales depend upon the direction of the instrument line-of-sight, as well as the numerical technique used to compute the variances. Waves propagating in horizontal directions perpendicular to the LOS are most visible, while those travelling parallel to it are strongly attenuated as a result of the averaging of positive and negative temperature perturbations along the LOS.

Radiances from both the limb-scanning and limb-tracking modes of operation are used. Limb-scanning variances are computed using data in the bottom portion of each scan and contain information about horizontal scales of < 90 km in the direction parallel to the

satellite track. Track variances are computed using all of the radiances after having first been Fourier-filtered in the along-track direction to retain only horizontal scales < 480 km. Systematic differences between the scan and track variances are found, which are believed to arise from changes in the vertical tilt angle of the LOS which is nearly fixed in limb-tracking mode but varies by several degrees over adjacent scan measurements. Consequently, the two datasets are treated independently. Limb-scanning observations constitute the bulk of the measurements and provide data from the launch of the satellite in September 1991 to July 1997 when the 63-GHz radiometer was switched off. The limb-tracking data covers a shorter period starting from December 1994.

The linear gravity wave model of A98 is used to aid in the interpretation of the MLS observations and to determine the degree to which horizontal variations in the observations at 38 km are indicative of gravity wave source variations in the troposphere. To simulate MLS's limb-tracking geometry and scale sensitivity, a three-dimensional wavenumber filter is employed. Winds and temperatures from the assimilated UKMO analyses, which correspond to the same time periods as the MLS observations, provide the background atmosphere. A horizontally-uniform momentum flux source spectrum containing a range of horizontal wavelengths and phase speeds is prescribed in the troposphere. This enables the effects of filtering by the background atmosphere to be isolated since horizontal variations in the simulated variances can only arise as a result of spatial variations in the background atmosphere. Gravity waves generated by sources such as convection or shear instability are represented using a horizontally-isotropic broad spectrum of horizontal wavelengths and phase speeds. Since the phase speed characteristics of these sources are not known, several different spectra are examined: these consist of a flat spectrum and two Gaussian-shaped spectra centered at zero phase speed. The other source spectrum represents orographically-generated gravity waves. Its distribution is very narrow in phase speed and is anisotropic in the horizontal direction.

The main conclusions are as follows:

(1) The spatial structure of the observed temperature variances is strongly correlated with the background winds as discussed by A98: the largest variances generally occur in regions where the winds are strongest. This follows from the instrument's wavenumber response and the gravity wave dispersion

relation which dictates that vertical wavelengths are proportional to Doppler-shifted phase speeds. This explains in large part why the maximum variances in summertime occur at the $\sim 5^\circ - 25^\circ$ latitude band where the stratospheric easterlies are strongest and why the longitudinally-dependent variations seen in the northern hemisphere winter correspond closely to the zonal wavenumber one modulation of the jet stream. These two regions (i.e., subtropical summer and midlatitude winter) are where the MLS variances are significantly above the noise level and are consequently the focus of this study.

(2) The mean variances in summertime exhibit distinct seasonal and geographical variations. The maxima are situated over the subtropical continents, namely southern Asia, North Africa and central North America in JJA, and southern Africa, northern Australia and Brazil in DJF. These features are observed in both the scan and track data. The standard deviation of the variances is found to be highly spatially correlated with the mean and exhibits values that are comparable to or larger than the means themselves.

(3) The longitudinal variations of the observed variances in the summer subtropics cannot be accounted for by changes in the background atmosphere and are therefore indicative of variations in tropospheric wave sources. The fact that the variance maxima are highly correlated with satellite measurements of outgoing-longwave radiation is strong evidence that deep convection is the source for these waves. The high degree of correlation is also an indication that the longest vertical wavelength waves are generated within the deepest convective clouds. This fact supports models that relate the depth of latent heating to the vertical wavelengths of the waves generated [Bergman and Salby, 1994; Alexander et al., 1995; Pandya and Alexander, 1999].

(4) The presence of large variances over North America in summer which are not associated with strong stratospheric winds indicates that waves with high ground-based phase speeds must be present. These features are quite robust since they appear in both the track and scan data. Strong convection over the Great Plains is the likely source mechanism.

(5) The maximum variance in southern hemisphere winter occurs over the tip of South America; a secondary broad maximum is found over the oceanic regions at 60°S . These features are seen in both the track and scan data. In northern hemisphere winter the locations of the track and scan mean variance maxima differ, but both lie over the continental

land masses. The standard deviations are considerably larger than the mean variances. Although the deviations tend to be largest over the continents, they do not always occur at the same geographic location as the means. This is particularly true in northern hemisphere winter. These differences in the spatial patterns in the northern hemisphere winter can be attributed to the much higher degree of variability in the background winds.

(6) The observed high-latitude variance peak in winter over the southern Andes and the Antarctic peninsula cannot be reproduced using a horizontally-uniform broad isotropic source spectrum. Model results using the narrow anisotropic spectrum show that the strong tropospheric and stratospheric westerlies at these latitudes are conducive to the generation and observability of orographically-generated gravity waves. This is further supported by the high correlation of the observed maximum and mountainous terrain. The high latitude northern hemisphere variances in winter, however, show a weaker correlation with topography.

(7) The model simulations indicate that the large standard deviations seen in the observed variances in the subtropics in summer cannot be caused by temporal variations in the background atmosphere and so must be indicative of source intermittency. The same cannot be said for high latitudes in winter since a time-varying winds and temperatures alone result in strong variability.

(8) The temperature variances are strongly dependent upon the orientation of the instrument's LOS as was shown by WW97. Both the track and scan variances are largest along the orbit track in which the instrument LOS is pointing eastward at high latitudes in winter and westward in the summertime subtropics.

(9) Use of the three-dimensional wavenumber response filter yields simulated variances that exhibit the same viewing-geometry dependence as the observations. This confirms the hypothesis of WW97 that differences in ascending- and descending-orbit (AD) variances occur because of differences in the alignment of the instrument LOS with respect to the gravity wave ridges and troughs. Moreover, our model results reveal that the differences between the AD variance increase as the phase speed distribution of the gravity wave source decreases. Thus, the flat spectrum, which contains the highest phase speeds, exhibits the smallest AD differences; the narrow anisotropic spectrum represents the other ex-

treme since these waves are only observable along a single orbit direction.

(10) Information about gravity wave phase speeds at the source heights is contained in both the AD variance ratios and the latitudinal width of the variance peaks. Comparison of the model ratios to the observations reveals that a fairly broad spectrum of phase speeds best characterizes the subtropical summer, which suggests that a source like deep convection generates a wide range of phase speeds. At high latitudes in the winter where the AD ratios are larger, a narrower spectrum better represents the observations. The actual values of the spectral widths, however, are not very meaningful since the shape of the spectra will not be the same as what we assumed. The model simulations also indicate that the latitudinal width of the variance peaks is related to the phase speed distribution at the source level. A broad momentum flux source spectrum produces filtered variances in the stratosphere that exhibit a relatively weak latitudinal dependence as occurs in the observations in the subtropics in summer, while a narrower spectrum results in sharply peaked variances as is observed in winter. This is in agreement with the AD ratios.

(11) The subtropical summertime variances can be explained fairly well without assuming any horizontal anisotropy in the source spectrum. Amplitude growth with height will have the effect of filling in weak spots in an anisotropic spectrum, so that source anisotropies are not likely to be a dominant factor unless there is a total absence of waves in some azimuths at the source level.

Acknowledgments.

This research was supported by the NASA New Investigators Program of Earth Sciences, UARS grant number NAFG-5-7090, and the Canadian Middle Atmosphere Modelling Project. Support for MJA was provided by the Physical Meteorology Program of the National Science Foundation (ATM-9896269). We would like to thank Gloria Manney for providing the gridded UKMO data. CM also expresses his thanks to Jim Holton, Takeshi Hironouchi, Joe Waters, and Bill Read for helpful discussions.

References

- Alexander, M. J., and L. Pfister, Gravity wave momentum flux in the lower stratosphere over convection, *Geophys. Res. Lett.*, **22**, 2029-2032, 1995.
- Alexander, M. J., J. R. Holton, and D. R. Durran, The gravity wave response above deep convection in a squall line simulation, *J. Atmos. Sci.*, **52**, 2212-2226, 1995.
- Alexander, M. J., and K. H. Rosenlof, Nonstationary gravity wave forcing of the stratospheric zonal mean wind, *J. Geophys. Res.*, **101**, 23465-23474, 1996.
- Alexander, M. J., Interpretations of observed climatological patterns in stratospheric gravity wave variance, *J. Geophys. Res.*, **103**, 8627-8640, 1998.
- Alexander, M. J., and T. J. Dunkerton, A spectral parameterization of mean-flow forcing due to breaking gravity waves, *J. Geophys. Res.*, 1999 (in press).
- Allen, S. J., and R. A. Vincent, Gravity wave activity in the lower atmosphere: seasonal and latitudinal variations, *J. Geophys. Res.*, **100**, 1327-1350, 1995.
- Bacmeister, J. T., Mountain-wave drag in the stratosphere and mesosphere inferred from observed winds and a simple mountain-wave parameterization scheme, *J. Atmos. Sci.*, **50**, 377-399, 1993.
- Bergman, J. W., and M. L. Salby, Equatorial wave activity derived from fluctuations in observed convection, *J. Atmos. Sci.*, **51**, 3791-3806, 1994.
- Dewan, E. M., R. H. Picard, R. R. O'Neil, H. A. Gardiner, and J. Gibson, MSX satellite observations of thunderstorm-generated gravity waves in mid-wave infrared images of the upper stratosphere, *Geophys. Res. Lett.*, **25**, 939-942, 1998.
- Dunkerton, T. J., and N. Butchart, Propagation and selective transmission of internal gravity waves in a sudden warming, *J. Atmos. Sci.*, **41**, 1443-1460, 1984.
- Eckermann, S. D., I. Hirota and W. K. Hocking, Gravity wave and equatorial wave morphology of the stratosphere derived from long-term rocket soundings, *Quart. J. Roy. Meteor. Soc.*, **121**, 149-186, 1994.
- Eckermann, S. D., On the observed morphology of gravity-wave and equatorial-wave variance in the stratosphere, *J. Atmos. Terr. Phys.*, **57**, 105-134, 1995.
- Eckermann, S. D., and P. Preusse, Global measurements of stratospheric mountain waves from space, *Science*, (accepted), 1999.
- Fetzer, E. J., J. C. Gille, Gravity wave variance in LIMS temperatures. Part I: Variability and comparison with background winds, *J. Atmos. Sci.*, **51**, 2461-2483, 1994.
- Fishbein, E. F., et al., Validation of UARS Microwave Limb Sounder temperature and pressure measurements, *J. Geophys. Res.*, **101**, 9983-10016, 1996.
- Fleming, E. L., S. Chandra, J. J. Barnett and M. Corney, Zonal mean temperature, pressure, zonal wind and geopotential height as functions of latitude, *Adv. Space Res.*, **10**, 11-59, 1990.
- Gossard, E. E., and W. H. Hooke, *Waves in the Atmosphere*, 456 pp., Elsevier, New York, 1975.
- Hamilton, K., Climatological statistics of stratospheric inertia-gravity waves deduced from historical rocket-sonde wind and temperature data, *J. Geophys. Res.*, **96**, 20831-20839, 1991.
- Hirota, I., Climatology of gravity waves in the middle atmosphere, *J. Atmos. Terr. Phys.*, **46**, 767-773, 1984.
- Jarnot, R. F., R. E. Cofield, J. W. Waters, D. A. Flower and G. E. Peckham, Calibration of the Microwave Limb Sounder on the Upper Atmosphere Research Satellite, *J. Geophys. Res.*, **101**, 9957-9982, 1996.
- Larsen, M. F., W. E. Swartz, and R. F. Woodman, Gravity-wave generation by thunderstorms observed with a vertically-pointing 430 MHz radar, *Geophys. Res. Lett.*, **9**, 571-574, 1982.
- Liebman, B., and C. A. Smith, Description of a complete (interpolated) outgoing longwave radiation data set, *Bull. Amer. Meteor. Soc.*, **77**, 1275-1277, 1996.
- Marks, C. J., and S. D. Eckermann, A three-dimensional nonhydrostatic ray-tracing model for gravity waves: formulation and preliminary results for the middle atmosphere, *J. Atmos. Sci.*, **52**, 1959-1984, 1995.
- McFarlane, N. A., The effect of orographically excited gravity wave drag on the general circulation of the lower stratosphere and troposphere, *J. Atmos. Sci.*, **44**, 1775-1800, 1987.
- McLandress, C., On the importance of gravity waves in the middle atmosphere and their parameterization in general circulation models, *J. Atmos. Sol. Terr. Phys.*, **60**, 1357-1383, 1998.
- Nastrom, G. D., T. E. Van Zandt, and J. M. Warnock, Vertical wavenumber spectra of wind and temperature from high-resolution balloon soundings over Illinois, *J. Geophys. Res.*, **102**, 6685-6701, 1997.
- Pandya, R. E., and M. J. Alexander, Linear stratospheric gravity waves above convective thermal forcing, *J. Atmos. Sci.*, **56**, 2434-2446, 1999.
- Rottger, J., Structure and dynamics of the stratosphere and mesosphere revealed by VHF radar investigations, *Pure Appl. Geophys.*, **118**, 494-527, 1980.
- Sato, K., H. Hashiguchi, and S. Fukao, Gravity waves and turbulence associated with cumulus convection observed with the UHF/VHF clear-air Doppler radars, *J. Geophys. Res.*, **100**, 7111-7119, 1995.
- Swinbank, R., and A. O'Neill, A stratosphere-troposphere data assimilation system, *Mon. Wea. Rev.*, **122**, 686-702, 1994.
- Tsuda, T., T. E. VanZandt, M. Mizumoto, S. Kato, and S. Fukao, Spectral analysis of temperature and Brunt-Vaisala frequency fluctuations observed by radiosondes, *J. Geophys. Res.*, **96**, 265-278, 1991.
- Wu, D. L., and J. W. Waters, Satellite observations of atmospheric variances: a possible indication of gravity waves, *Geophys. Res. Lett.*, **23**, 3631-3634, 1996a.

Wu, D. L., and J. W. Waters, Gravity-wave-scale temperature fluctuations seen by the UARS MLS, *Geophys. Res. Lett.*, 23, 3289-3292, 1996b.

Wu, D. L., and J. W. Waters, Observations of gravity waves with the UARS Microwave Limb Sounder, in *Gravity Wave Processes and Their Parameterization in Global Climate Models*, edited by K. Hamilton, pp. 103-120, Springer-Verlag, Berlin, 1997.

C. McLandress, Department of Earth and Atmospheric Science, York University, Toronto, Ontario, Canada.

; revised ; accepted .

Table 1. Number of days of data used in the limb-tracking and limb-scanning variance climatologies for the north- and south-looking viewing periods of DJF and JJA.

Season	View	Track	Scan
DJF	north	57 days	277 days
DJF	south	12 days	125 days
JJA	north	12 days	97 days
JJA	south	18 days	255 days

Table 2. Approximate horizontal direction of MLS's line-of-sight for the four different viewing configurations.

	ascending	descending
north-looking	NW	NE
south-looking	SE	SW

Table 3. Ratios of the ascending- (A) and descending- (D) orbit zonal-average variances at 38 km for the MLS limb-tracking observations and the model simulations using the flat, $c_w = 50$ m/s and $c_w = 20$ m/s source spectra. The numbers in brackets denote the observed ratios at the longitude of the maximum. The noise, which is estimated at 0.011°K^2 , has been removed from the MLS variances before computing the ratios.

Latitude	season	ratio	MLS	flat	$c_w = 50$ m/s	$c_w = 20$ m/s
55°N	DJF	D/A	4.4 (6.0)	1.2	1.6	5.3
15°N	JJA	D/A	1.5 (2.1)	1.2	1.7	8.1
15°S	DJF	A/D	1.7 (1.9)	1.2	1.8	7.9
55°S	JJA	A/D	4.8 (10.1)	1.3	2.0	4.5

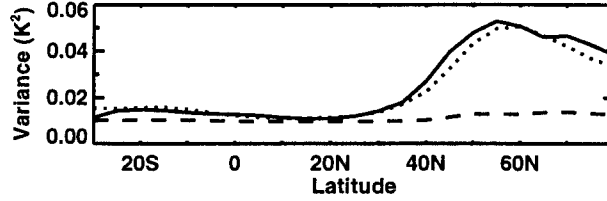


Figure 1: Zonal-average MLS temperature variances at 38 km for the six-point limb-scanning data (solid), six-point limb-tracking data (dashed) and 480-km limb-tracking data (dots). The variances are averaged over a 22-day period in DJF (1996-97) when track and scan observations were made on alternate days. Results are shown for north-looking descending orbits.

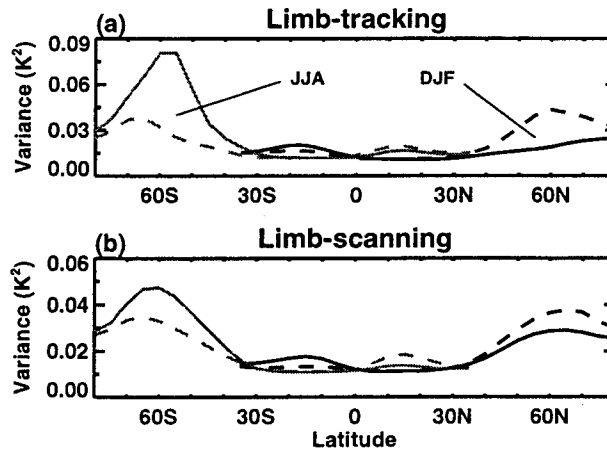


Figure 2: Zonal-average MLS temperature variances at 38 km for ascending orbits (solid) and descending orbits (dashed) for: (a) limb-tracking and (b) limb-scanning data. The black and gray curves denote observations for the north-looking days of DJF and the south-looking days of JJA, respectively.

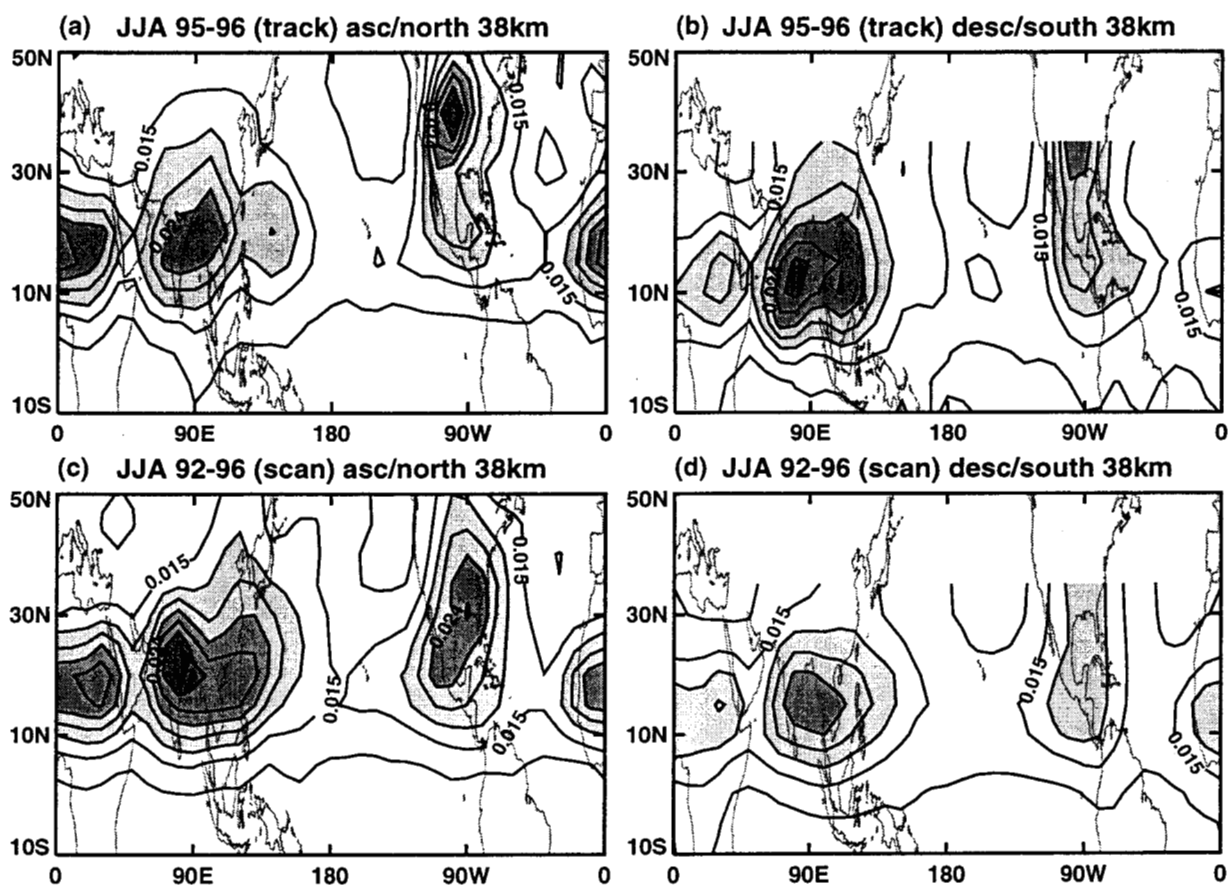


Figure 3: MLS temperature variances at 38 km for northern hemisphere summer. Limb-tracking data for: (a) north-looking ascending orbits and (b) south-looking descending orbits. Panels (c) and (d) are the same but for limb-scanning data. A contour interval of 0.003°K^2 is used.

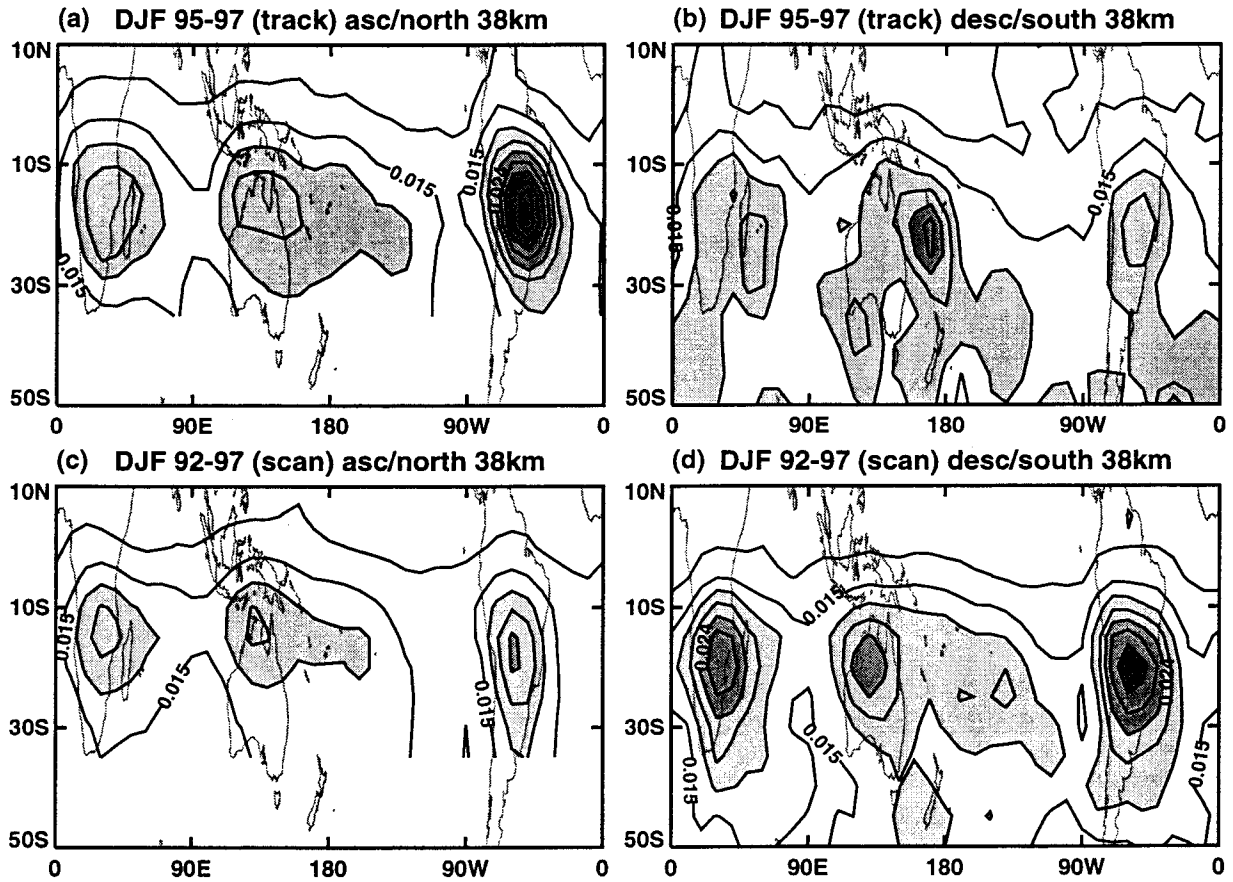


Figure 4: MLS temperature variances at 38 km for southern hemisphere summer. Limb-tracking data for: (a) north-looking ascending orbits and (b) south-looking descending orbits. Panels (c) and (d) are the same but for limb-scanning data. A contour interval of 0.003°K^2 is used.

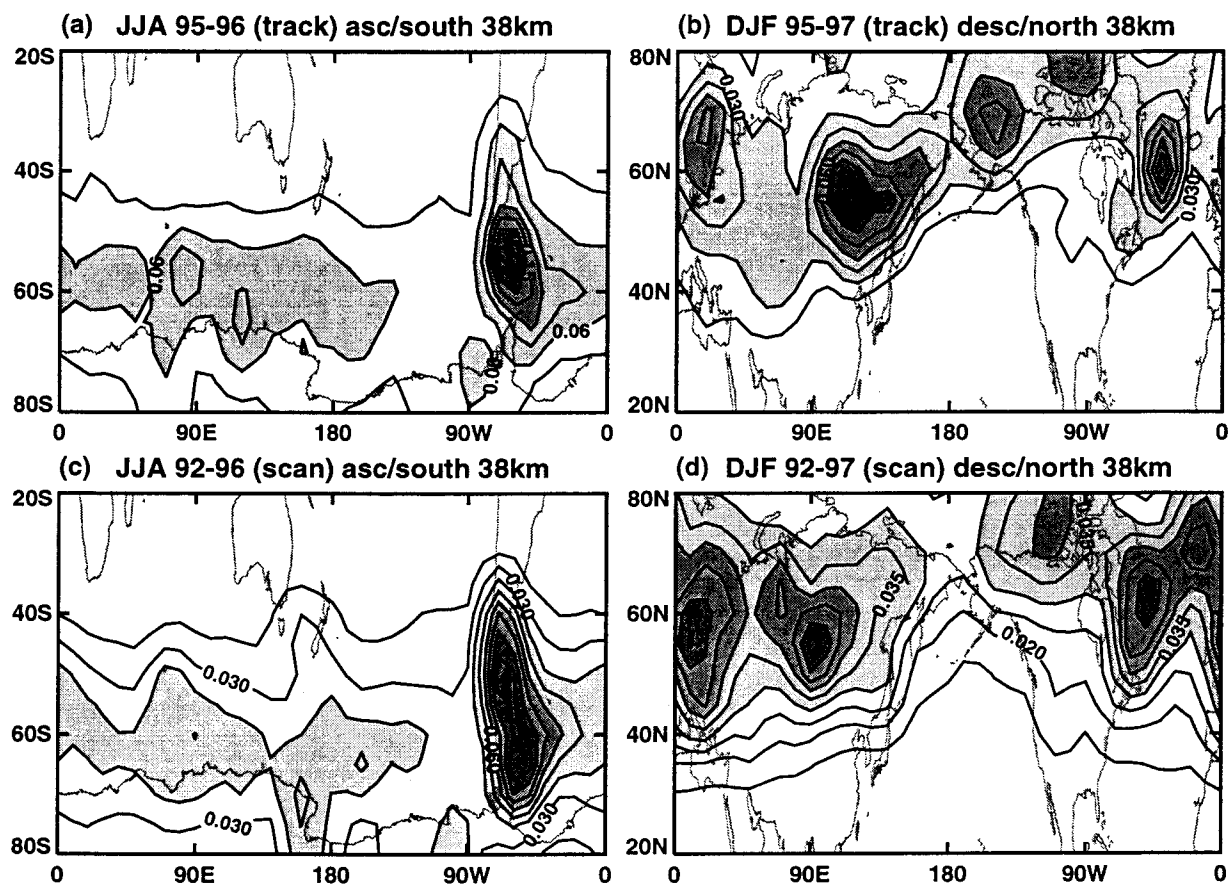


Figure 5: MLS temperature variances at 38 km for winter. Limb-tracking data for: (a) south-looking ascending orbits (JJA) and (b) north-looking ascending orbits (DJF). Panels (c) and (d) are the same but for limb-scanning data. Contour intervals of 0.03, 0.01, 0.01 and 0.005 K^2 are used in panels (a), (b), (c) and (d), respectively.

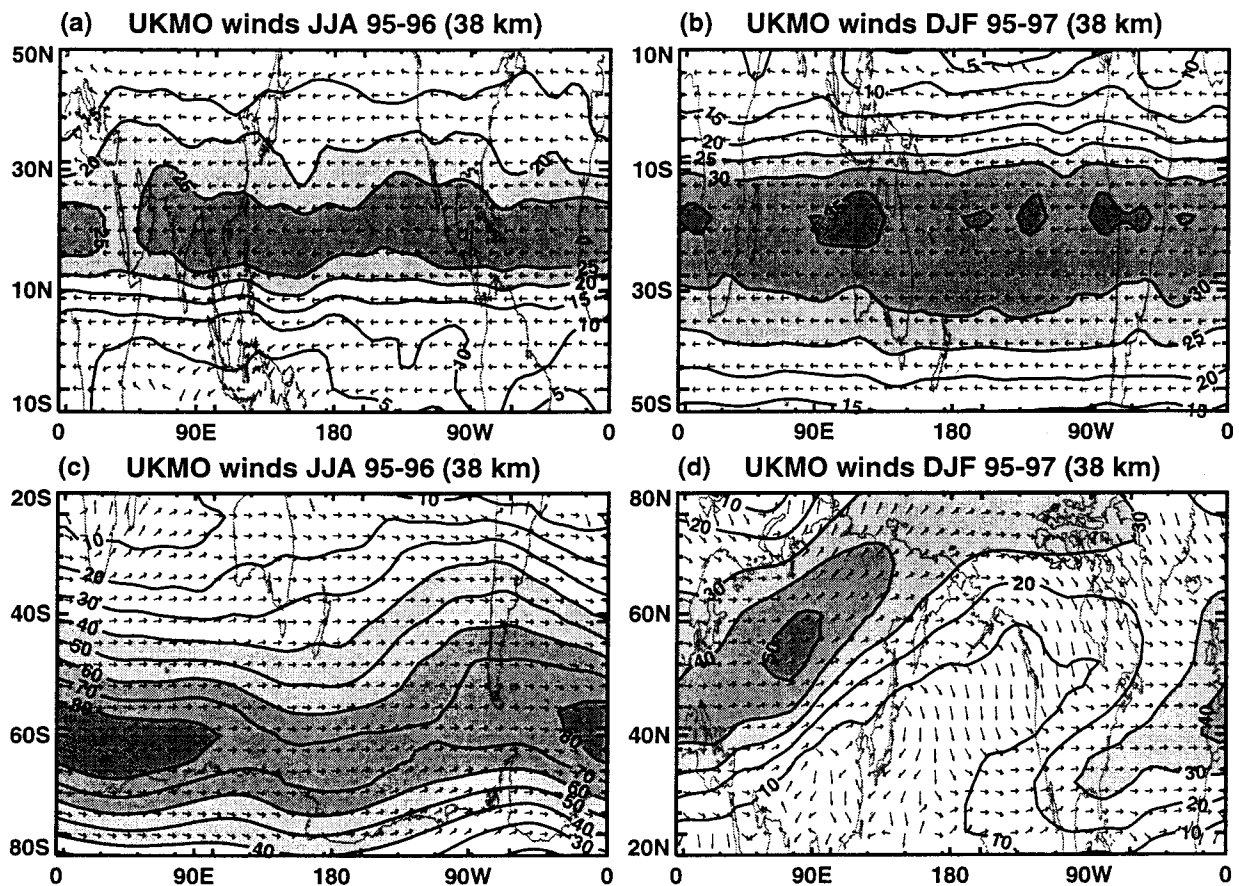


Figure 6: UKMO horizontal winds at 38 km time averaged for the days corresponding to the MLS limb-tracking observations (south-looking days for JJA and north-looking days for DJF). Wind speed (m/s) is denoted by the contours and direction by the unit vectors. Note that the shading interval differs in each panel.

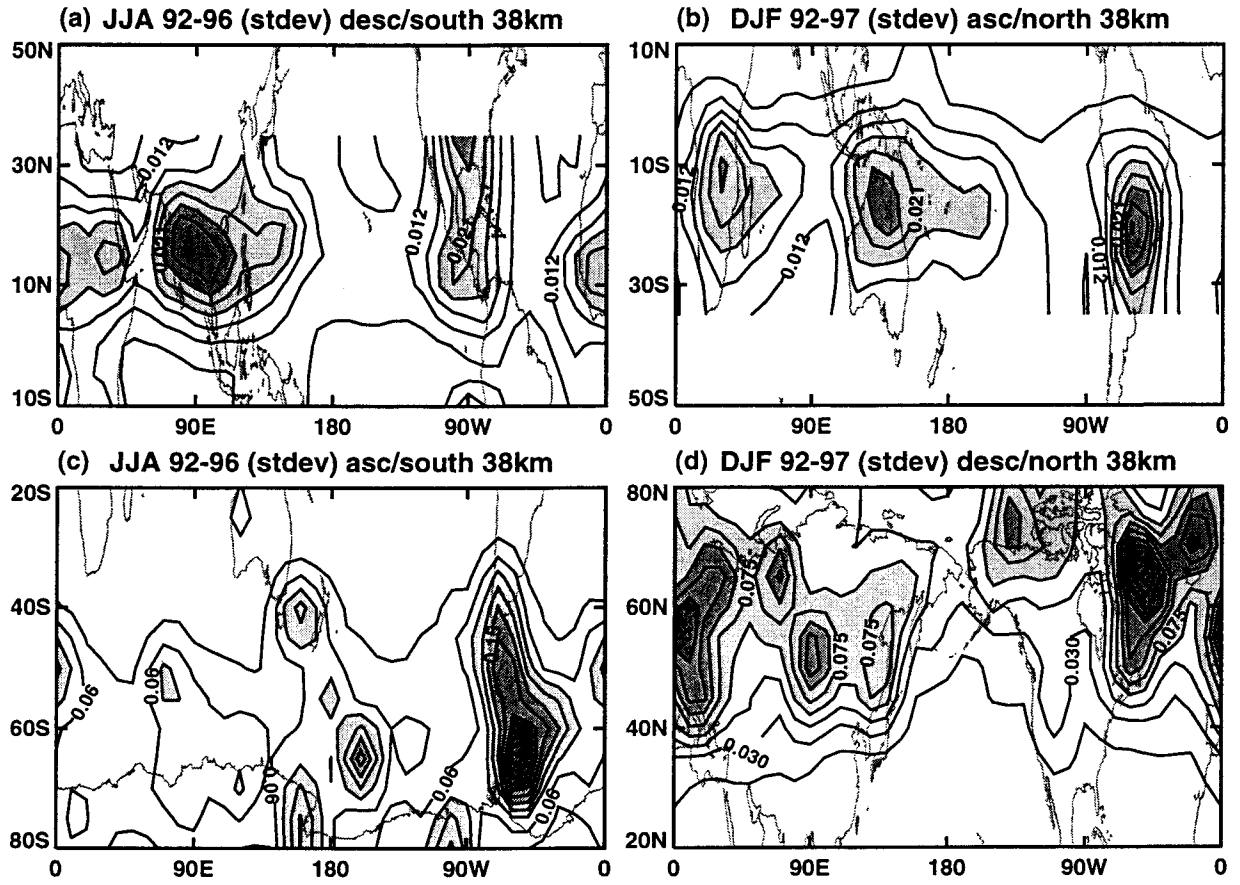


Figure 7: Standard deviations of the MLS limb-scanning temperature variances about the seasonal means shown in Figures 3d, 4c, 5c and 5d. Contour intervals of 0.003, 0.003, 0.03 and 0.015 $^{\circ}\text{K}^2$ are used in panels (a), (b), (c) and (d), respectively.

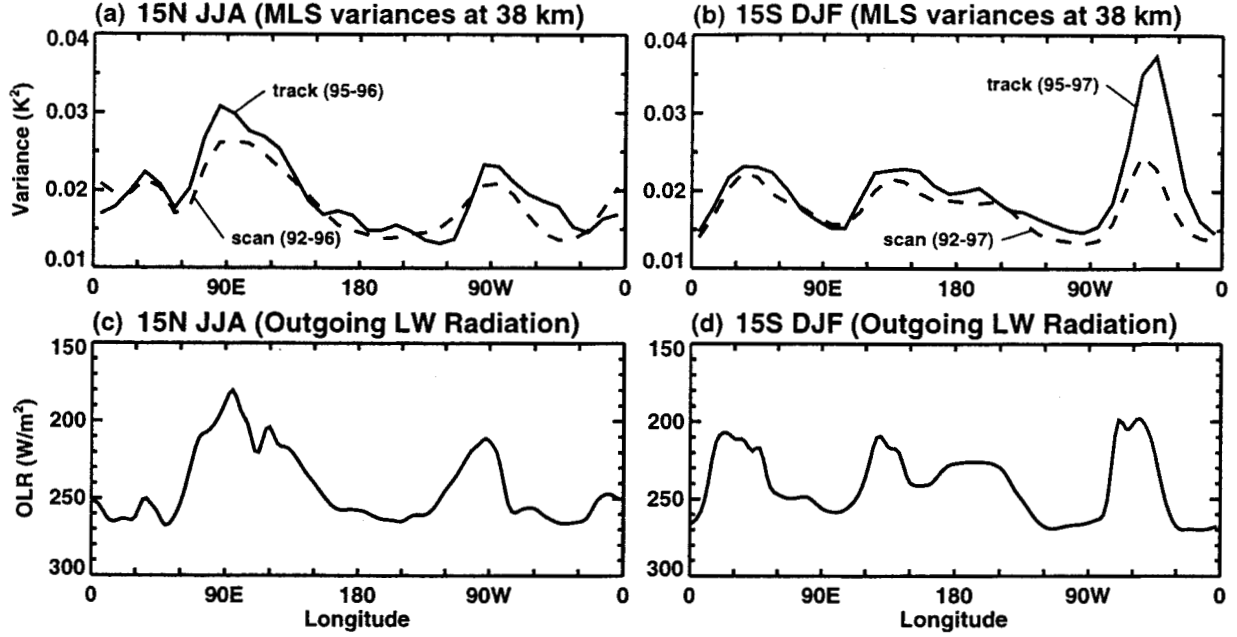


Figure 8: (a) MLS limb-tracking and limb-scanning temperature variances at 38 km for JJA at 15°N for south-looking descending orbits. (b) Same but for DJF at 15°S for north-looking ascending orbits. (c) Outgoing longwave radiation for JJA (1992-96) at 15°N from *Liebmann and Smith* [1996], smoothed twice in longitude using a 1:2:1 three-point filter. (d) Same but for DJF at 15°S.

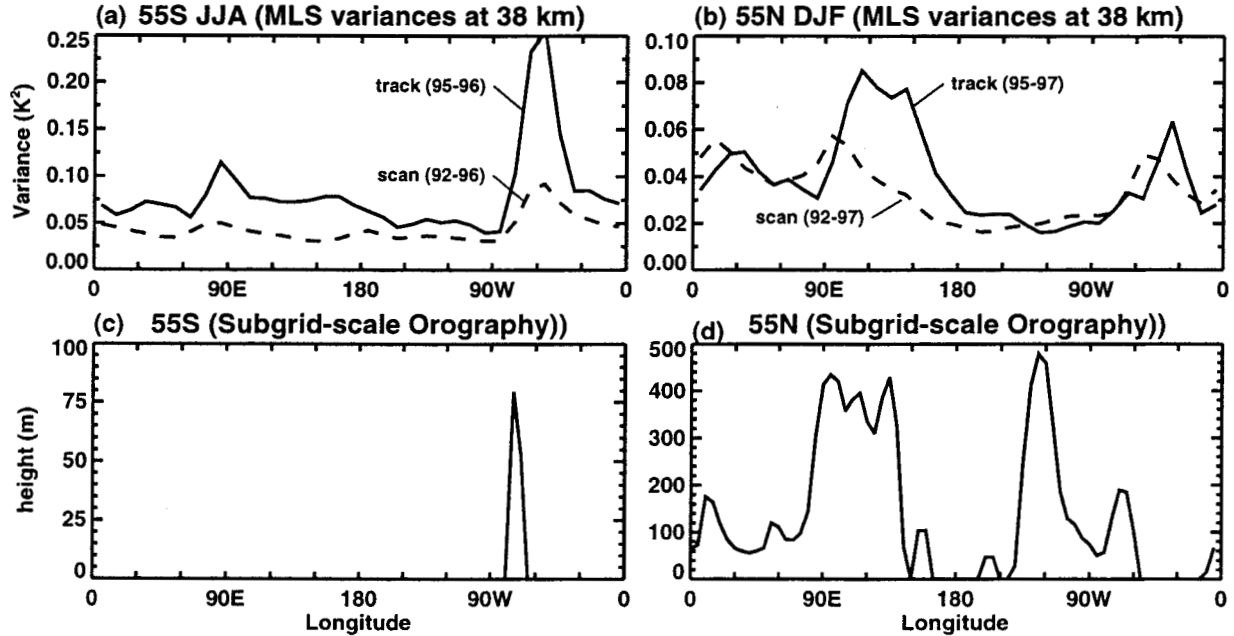


Figure 9: (a) MLS limb-tracking and limb-scanning temperature variances at 38 km for JJA at 55°S for south-looking ascending orbits. (b) Same but for DJF at 55°N for north-looking descending orbits. (c) Twice the standard deviation of the subgrid-scale orography used for the gravity wave drag parameterization of *McFarlane* [1987] for a model resolution of $\sim 5^\circ$. (d) Same but for 55°N.

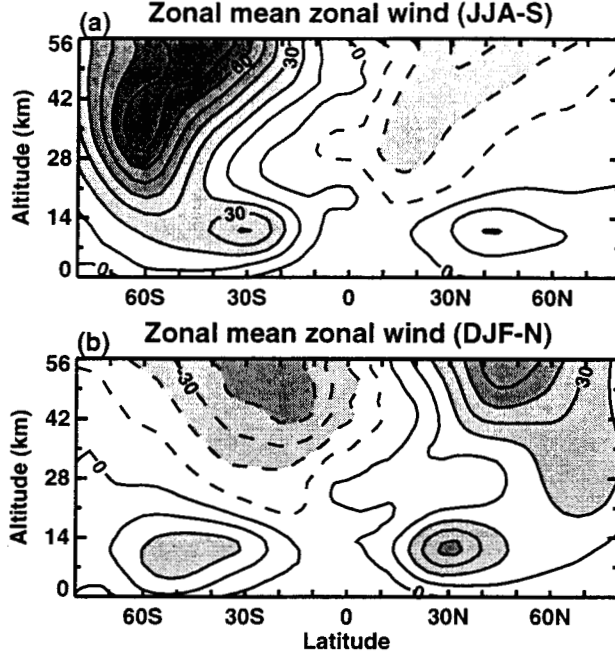


Figure 10: Zonal-average zonal winds in m/s for the UKMO background atmospheres JJA-S and DJF-N shown in Figure 6.

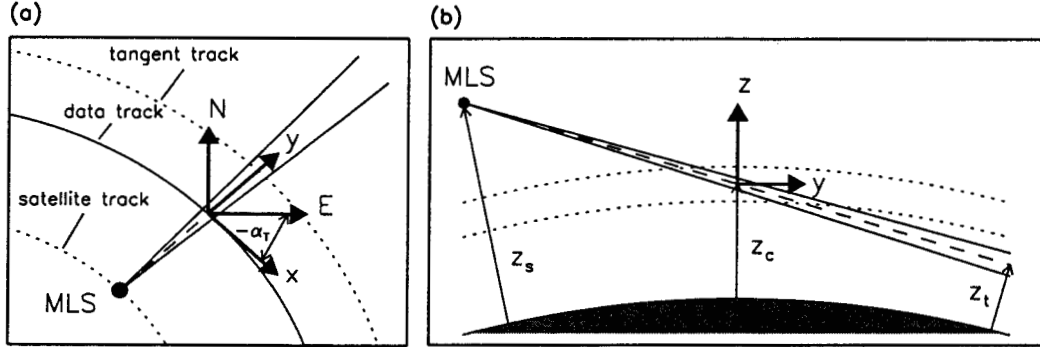


Figure 11: (a) Horizontal and (b) vertical geometry used to define the MLS filter. The thick arrows indicate the along-track (x), across-track (y) and vertical (z) coordinate system, which is centered at the point where the instrument LOS (long dashes) intersects the height where the channel saturates (z_c). The saturated radiance measured by MLS is emitted from the volume of atmosphere centered at the origin of this coordinates system. The data track angle (α_T) is positive counterclockwise from the east. The heights of the tangent point and satellite are given by z_t and z_s , respectively. The solid lines on either side of the LOS indicate the instrument beam width. The horizontal configuration shown here corresponds to a north-looking descending orbit viewing geometry.

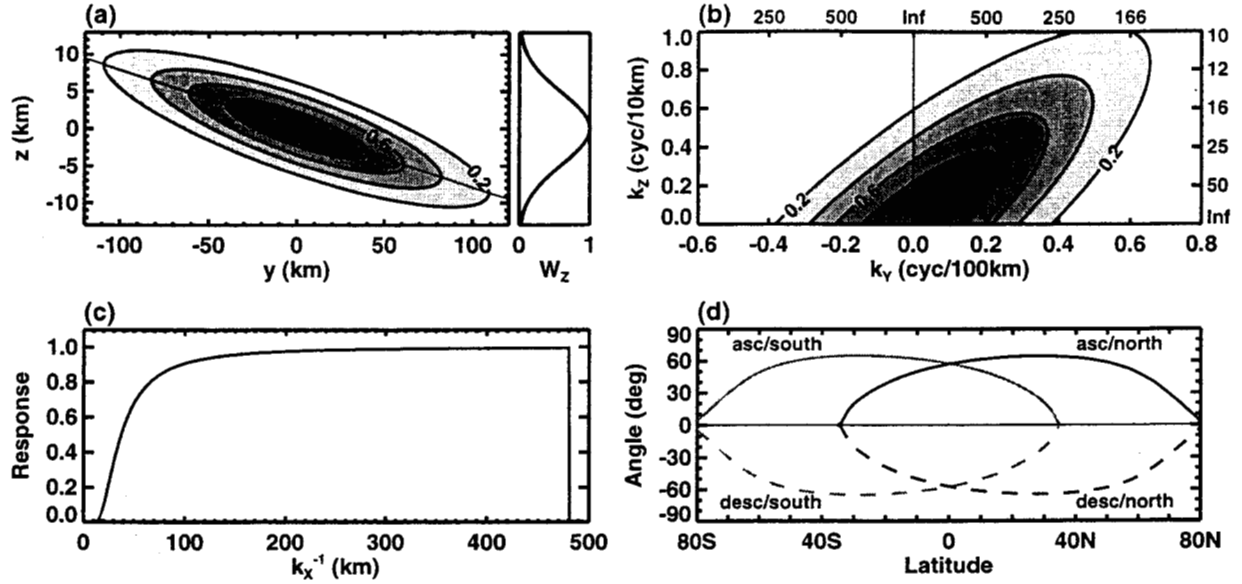


Figure 12: (a) Idealized two-dimensional temperature weighting function for channels 3 and 13 constructed from the weighting function shown at right. The thin solid line denotes the instrument LOS. (b) Normalized across-track temperature response as a function of the across-track and vertical wavenumbers, k_y and k_z . The corresponding wavelengths in kilometers are marked along the opposite axes. (c) Normalized along-track temperature response as a function of the along-track wavelength ($1/k_x$). (d) Data track angle (α_T) for the ascending and descending orbits for both the north- and south-looking yaw directions.

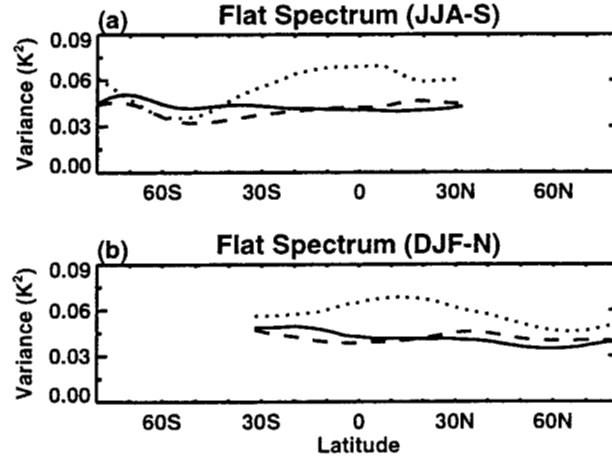


Figure 13: Zonal-average temperature variances at 38 km computed using the flat spectrum and the (a) JJA-S and (b) DJF-N background atmospheres. The ascending and descending orbit filter results are given by the solid and dashed lines, respectively; the unfiltered results are denoted by the dotted lines. South-looking geometry is used in panel (a), north-looking geometry is used in panel (b). The filtered and unfiltered results are multiplied by 0.4 and 0.02, respectively.

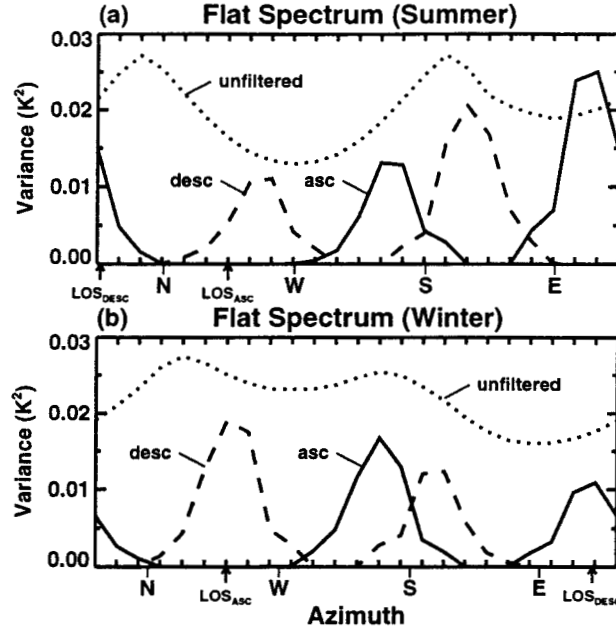


Figure 14: Zonal-average temperature variances at 38 km computed using the flat spectrum and the DJF-N background atmosphere and plotted as a function of the horizontal propagation direction at (a) 16°S and (b) 56°N. Twenty-four azimuths are used; the first azimuth is aligned with the ascending orbit data track. Results are shown for both the ascending- and descending-orbit configurations of the filter. Arrows indicate the direction of the LOS. N, W, S and E denote the 4 cardinal points of the compass. The unfiltered variances have been multiplied by 0.15 and 0.07 in panels (a) and (b), respectively.

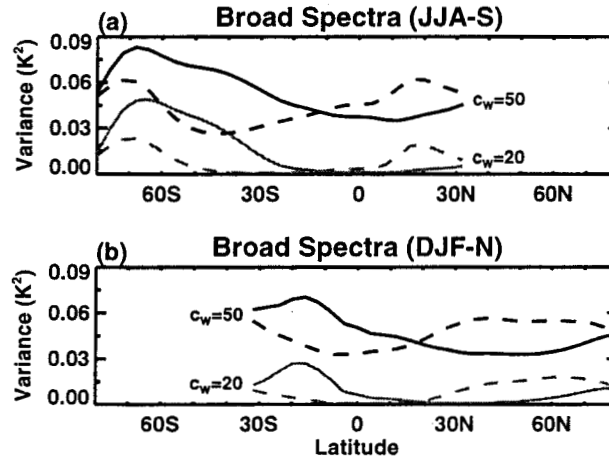


Figure 15: Zonal-average temperature variances at 38 km computed using the $c_w = 20$ and 50 m/s spectra and the (a) JJA-S and (b) DJF-N background atmospheres. The ascending and descending orbit filter results are given by the solid and dashed lines, respectively. Filter geometry same as in in Figure 13. The results are multiplied by 0.5.

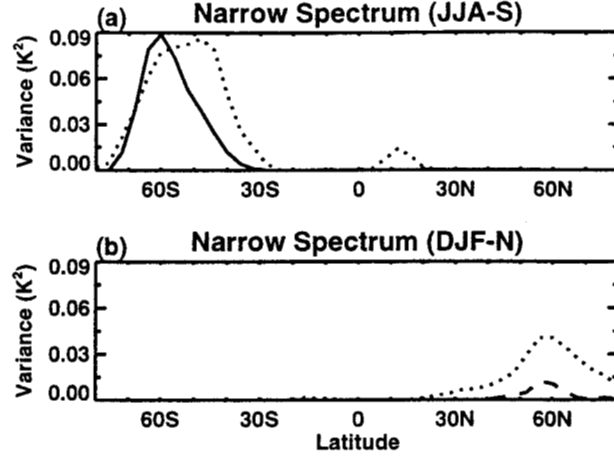


Figure 16: Zonal-average temperature variances at 38 km computed using the narrow spectrum and the (a) JJA-S and (b) DJF-N background atmospheres. The ascending and descending orbit filter results are given by the solid and dashed lines, respectively; the unfiltered results are denoted by the dotted lines. Filter geometry same as in Figure 13. The filtered and unfiltered results are multiplied by 0.2 and 0.02., respectively.

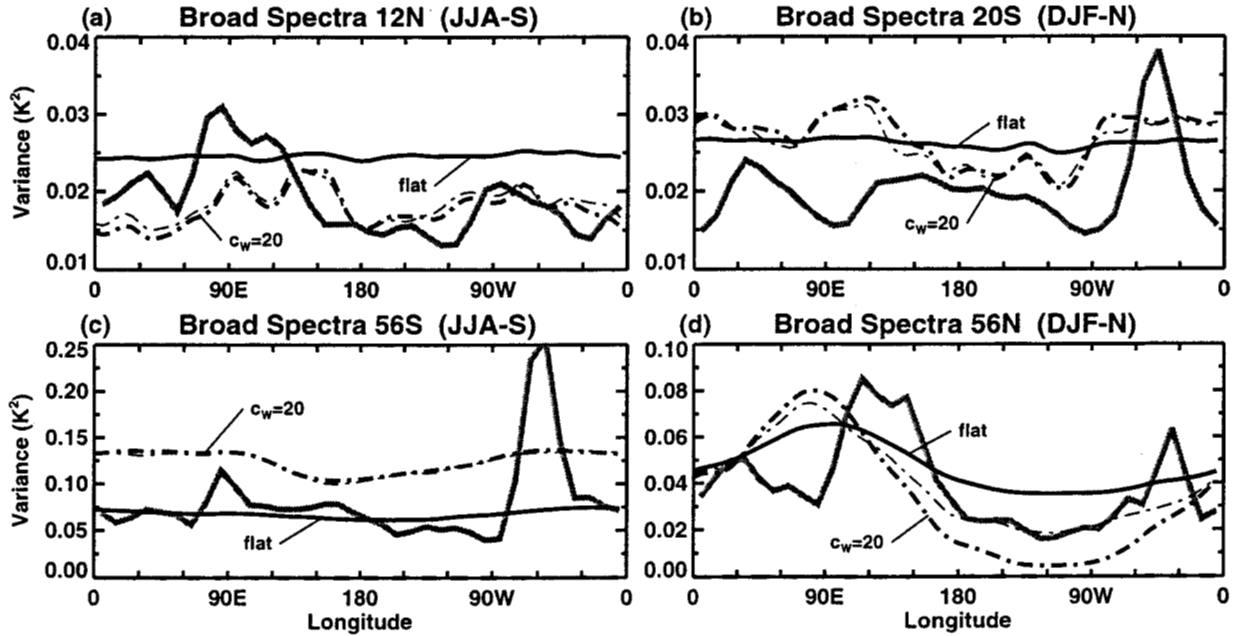


Figure 17: Filtered temperature variances at 38 km computed using the flat (solid) and $c_w = 20$ m/s (thick dashed-dotted line) spectra and the JJA-S and DJF-N background atmospheres. (a) JJA at 12°N (south-looking descending orbits), (b) DJF at 20°S (north-looking ascending orbits), (c) JJA at 56°S (south-looking ascending orbits), and (d) DJF at 56°N (north-looking descending orbits). The thin dashed-dotted line denotes the time-averaged variances for the $c_w = 20$ m/s spectrum computed using the daily UKMO background winds and temperatures. The MLS observations are indicated by the gray curves. Results for the flat spectrum are multiplied by 0.25 in panels (a) and (b), 0.75 in panel (c), and 0.5 in panel (d). Results for the $c_w = 20$ m/s spectrum are multiplied by 0.75 in panel (a), 0.5 in panels (b) and (c), and 1.0 in panel (d).

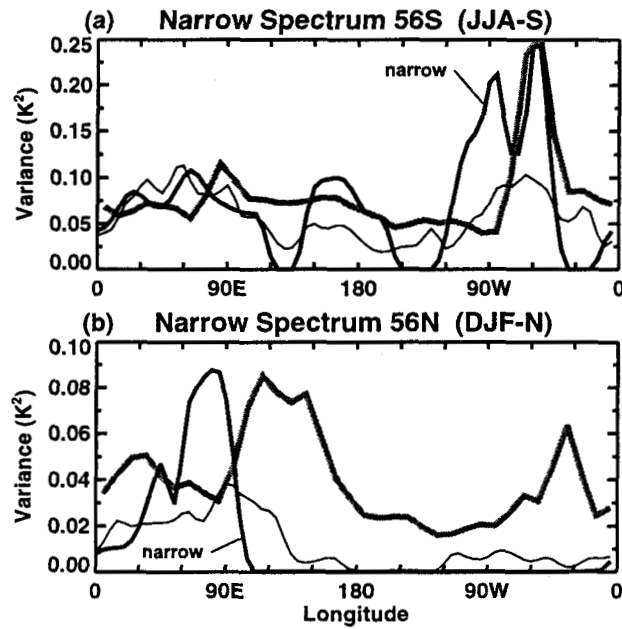


Figure 18: Filtered temperature variances at 38 km computed using the narrow spectrum. (a) JJA at 56°S (south-looking ascending orbits) and (b) DJF at 56°N (north-looking descending orbits). The thick black lines denote the results obtained using the time-averaged UKMO background atmospheres; the thin lines denote the time-averaged variances computed using the daily background winds and temperatures. The MLS observations are indicated by the gray curves. The filtered variances are multiplied by 0.2.